BOOK OF EXTENDED ABSTRACTS

THE 42nd ANNUAL SYMPOSIUM ON POLYMER SCIENCE/ENGINEERING

University of Waterloo
Waterloo, Ontario

September 2nd, 2020

INSTITUTE FOR POLYMER RESEARCH

UNIVERSITY OF WATERLOO

The Institute for Polymer Research would like to thank the sponsors for their support of the symposium.

UNIVERSITY OF WATERLOO
FACULTY OF SCIENCE

UNIVERSITY OF WATERLOO
FACULTY OF ENGINEERING

UNIVERSITY OF
WATERLOO
OFFICE OF RESEARCH

UNIVERSITY OF WATERLOO
FACULTY OF SCIENCE
Department of Chemistry

UNIVERSITY OF WATERLOO
FACULTY OF ENGINEERING
Department of Chemical Engineering

2020

PROGRAM

INSTITUTE FOR POLYMER RESEARCH
CELEBRATING 35 YEARS OF OFFICIAL INSTITUTE STATUS
FORTY-SECOND ANNUAL SYMPOSIUM
ON POLYMER SCIENCE/ENGINEERING 2020
University of Waterloo, Waterloo, Ontario
Wednesday, September 2, 2020

12:50	**Welcome and Opening Remarks**
1:00 – 1:20	**Janine Thoma [Prof. Duhamel]** Persistence Length of Polymeric Bottle Brushes Determined by Pyrene Excimer Fluorescence **(Winner of 2020 IPR Award for Academic Excellence in Polymer Science/Engineering)**
1:20 – 1:40	**Elnaz Esmizadeh [Prof. Mekonnen]** Degradation behavior of polypropylene during reprocessing and its biocomposites: thermal and oxidative degradation kinetics
1:40 – 2:20	**5-Min. Mini Presentations** **1) Sainiwetha Saihrishnan [Prof. Mekonnen]** Thermo-mechanical Degradation of Polypropylene-Low Density Polyethylene blend system after multiple extrusion **2) Javan Buratynski [Prof. Schipper]** Using Degradable Polymers to Separate Carbon Nanotubes **3) Abdullah Ba Salem [Prof. Duhamel]** Determination of Aggregation Number for Pyrene-labeled Gemini Surfactants **4) Kristijan Lulic [Prof. Duhamel]** Self-Association of Oligoquinoline Foldamers Probed by Fluorescence Anisotropy **5) Hunter Little [Prof. Duhamel]** Progress in Instrumentation for Time-resolved Fluorescence Anisotropy **6) Franklin Frasca [Prof. Duhamel]** Relating Pyrene Excimer Fluorescence to Conformation in Pyrene-Labeled Polyamines **7) Tiana Trumpur [Prof. Forrest]** Solvent Induced Nanoscopic Roughness on Glassy Polymer Thin Films **8) Minghui Liu (Prof. Zhao)** Antimicrobial Activity of Quaternary Ammonium Compound/Polyurethane [QAC/PU] Colloidal Complex Film Based on Synergetic Release Killing and Contact Killing Mechanisms
2:20 – 2:40	**Remi Casier [Prof. Duhamel]** Copolymerization and its Effects on Polymer Dynamics in Solution
2:40 – 3 :00	Break

Mini-Symposium on Modification, Characterization, and Applications of Polysaccharides

3:00 - 3:20	**Chunxia Tang [Prof. Tam]** Functionalized Cellulose Aerogel Beads for Heavy Metal Ions Removal **(Winner of the 2020 IPR Award for Academic Excellence in Polymer Science/Engineering)**
3:20 – 3:40	**Natun Dasgupta [Prof. Gauthier]** Thermoresponsive Starch Nanoparticles for Oil Recovery from Tar Sands
3:40 – 4:00	**<u>5-Min. Mini Presentations</u>** **9) Maryam Bagheri [Prof. Simon]** Polysaccharide-Ionic Liquid corrosion inhibitors **10) Ewomazino Ojogbo [Prof. Mekonnen]** Effects of fabrication method on the dispersion of CNCs in highly crosslinked rubber composites **11) Sanjay Patel [Prof. Duhamel]** Pyrene-labeled Starch Nanoparticles as Fluorescent Sensors for Explosive Detection **12) Donghan Liu [Prof. Duhamel]** Synthesis and Characterization of Furan Based Non-ionic Surfactant (FBNIOS)
4:00 – 4:20	**Joanne Fernandez [Prof. Gauthier]** Grafting of Starch Using a Complex Initiation System of CAN-KPS
4:20 – 4:40	**Muhammad Shahidul Islam [Prof. Tam]** Cellulose Nanomaterials: Synthesis, Properties, and Applications
4:40 - 5:00	**Damin Kim [Prof. Duhamel]** Better Understanding the Structure of Glycogen with Pyrene Excimer Fluorescence
5:00	**Closing Remarks**

EXTENDED ABSTRACTS

Janine Thoma
Chemistry
Waterloo

Persistence Length of Polymeric Bottle Brushes Determined by Pyrene Excimer Fluorescence

Winner of the 2020 IPR Award for Academic Excellence in Polymer Science/Engineering

Investigating the Conformation and Flexibility of Poly[oligo(ethylene glycol) Methacrylate] Polymeric Bottle Brushes in Solution

Janine Lydia Thoma and Jean Duhamel*

Institute for Polymer Research, Waterloo Institute for Nanotechnology, Department of Chemistry, University of Waterloo, ON N2L 3G1, Canada

Introduction

Polymer architecture is a key component in the design of a polymer because it dictates its physical properties and consequently, its desired applications. Branched polymers constitute a large family of macromolecules with complex architectures that can be separated into four main categories: star, dendritic and hyper-branched, brush, and network/gel polymers. This study focuses on the third category, namely brush polymers. Developments in the synthesis of brush polymers were spearheaded by the growing number of their applications. For example, they are used for drug delivery in the biomedical industry and to prepare new super-soft materials.[1,2] Brush polymers, also called polymeric bottle brushes (PBBs), offer functionality with respect to backbone and macromonomer chemical composition which allows for their customization depending on the specific property requirements of a given application. What gives a PBB its unique properties are its high grafting density and high degree of polymerization.

Contrary to studies of PBBs by microscopy where the macromolecule is adsorbed onto a 2-D surface, the characterization of PBBs in solution is of interest because it allows scientists to probe the flexibility of these densely packed systems in their native conformation. A PBB will adopt a different conformation, either a polymer coil or an extended rod, depending on whether it is prepared with a short or long macromonomer, respectively. The Kratky-Porod (KP) Worm-like chain model enables the derivation of Equation 1 which accounts for the relative extension of a polymer by relating its average end-to-end distance, r_{EE}, to its persistence length, l_p.

$$r_{EE}^2 = 2l_p Nb - 2l_p^{\,2}\left[1 - \exp(-Nb / l_p)\right] \quad (1)$$

In Equation 1, N and b are the number of bonds and the bond length, respectively. l_p quantifies the bending stiffness of a polymer and represents the characteristic length required to decorrelate the orientation of the tangent to the contour length of the main chain from its original orientation as shown in Equation 2. In Equation 2, $\theta(x)$ represents the angle between the tangent at the original position ($x = 0$) and at a position x along the chain contour length. l_p is equal to twice the Kuhn length, l_K. A polymer in an extended conformation, such as a PBB with long sidechains, will have a larger l_p than a polymer in a coil conformation, such as a PBB with short sidechains. A variety of techniques can be used to calculate l_p for a polymer, including static light scattering (SLS), small angle X-ray scattering (SAXS), small angle neutron scattering (SANS), atomic force microscopy (AFM) for a 2D worm-like chain adsorbed on a flat substrate, and for the first time in the scientific literature, pyrene excimer fluorescence (PEF).

$$< \cos[\theta(x)] > = \exp(-x / l_p) \quad (2)$$

In order to use PEF to determine l_p for a series of PBBs, small quantities of the macromonomers 1-pyrenemethoxy-penta(ethylene glycol) methacrylate ($PyEG_5MA$) was copolymerized with a series of methyl ether oligo(ethylene glycol) methacrylates (EG_xMA with x = 0, 3, 5, 7, 9, and 19) to yield a series of pyrene-labeled PBBs (Py-PEG_xMA). In turn, this report will illustrate how a combination of PEF, the fluorescence blob model (FBM),[3] and the KP model can be applied to calculate l_p for the Py-PEG_xMA samples as a function of side chain length (x). This study takes advantage of the fact that the scaling laws describing the properties of an entire polymer can be applied to sub-volumes of the polymer coil referred to as *blobs*. *Blobs* are often used in polymer physics to break down a polymer into even sub-volumes.[4] Within the framework of the FBM, a *blob* is defined as the volume probed by an excited pyrene and it is defined by its number of structural units N_{blob}. Application of the KP model to the *blobs* derived from the FBM, allows l_p to be calculated for each Py-PEG_xMA sample as shown in Equation 3.

$$r^2_{EE,blob} = 2l_p N_{blob} b - 2l_p{}^2\left[1-\exp(-N_{blob} b / l_p)\right] \quad (3)$$

In Equation 2, $r_{EE,blob}{}^2$, N_{blob}, and b represent the averaged squared end-to-end distance of the polymer segment inside a *blob*, the number of structural units encompassed inside a *blob* obtained with the FBM, and the length added to the main chain contour length by one macromonomer, respectively. Since the same $PyEG_5MA$ macromonomer was used for each Py-PEG_xMA sample, an excited pyrene probed the same volume during its lifetime resulting in a constant $r_{EE,blob}{}^2$ for each sample as depicted in Figure 1. Since $r_{EE,blob}{}^2$ could be determined for a fully extended Py-PEG_xMA with x = 19, Equation 3 was applied to calculate l_p for each Py-PEG_xMA sample.

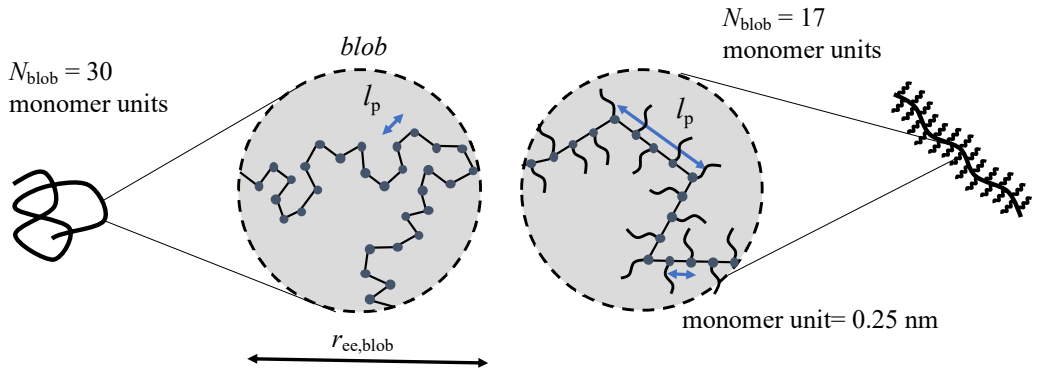

Figure 1. Random coil (left) and extended (right) polymer conformations in solution.

Experimental Procedure

The synthesis of a Py-PEG_xMA sample begins by preparing the pyrene labeled macromonomer ($PyEG_5MA$) (Scheme 1). The chemical composition of Py-EG_5MA was confirmed by ^1H NMR. Py-EG_5MA was then copolymerized by conventional radical chain polymerization in tetrahydrofuran (THF) with the methyl ether oligo(ethylene glycol) methacrylate (EG_xMA) macromonomers using a grafting through technique and azobisisobutyronitrile (AIBN) as the initiator to obtain the Py-PEG_xMA samples.

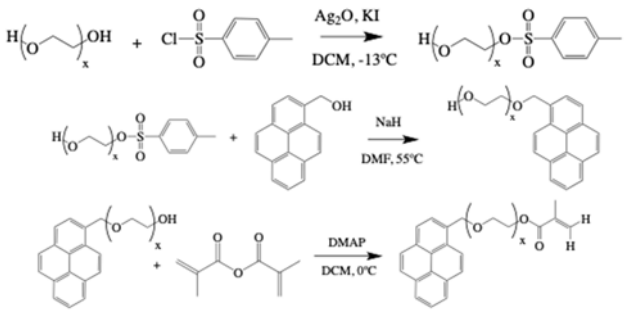

Scheme 1. Synthesis of the Py-EG$_5$MA macromonomer.

The Py-PEG$_x$MA samples were characterized using gel permeation chromatography (GPC) to obtain their number (M_n) and weight (M_w) average molecular weight, and polydispersity ($Đ$) as well as atomic force microscopy (AFM) to visualize the shape of the Py-PEG$_{19}$MA samples.

Table 1. Chemical structure of each Py-PBB and the number of atoms in each side chain, N_S.

Sample	Py-PEG$_0$MA	Py-PEG$_3$MA	Py-PEG$_5$MA	Py-PEG$_7$MA	Py-PEG$_9$MA	Py-PEG$_{19}$MA
Structure	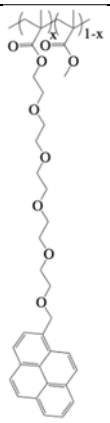	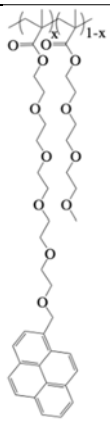	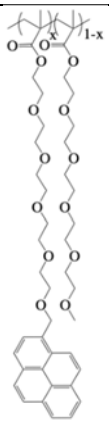	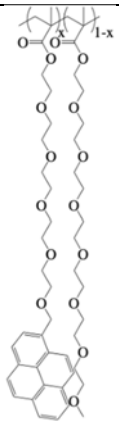		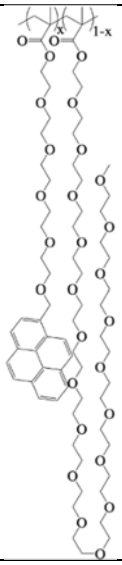
N_S	3	12	18	21	30	60

Results and Discussion

Six Py-PEG$_x$MA samples were prepared by conventional radical copolymerization of PyEG$_5$MA and different EG$_x$MA macromonomers to yield the chemical structures shown in Table 1. Each Py-PEG$_x$MA sample was prepared with 4-5 different pyrene contents. Each polymer was characterized using gel permeation chromatography (GPC) to determine their absolute M_n and M_w in dimethylsulfoxide (DMSO). Their degrees of polymerization were found to be greater than 100.

The time-resolved fluorescence decays of all Py-PEG$_x$MA samples were acquired in DMSO. They were analyzed according to the FBM to yield N_{blob} and the N_{blob} value averaged over all pyrene contents, $< N_{blob} >$, was plotted as a function of the number of atoms in the side chain (N_S) in Figure 2A.

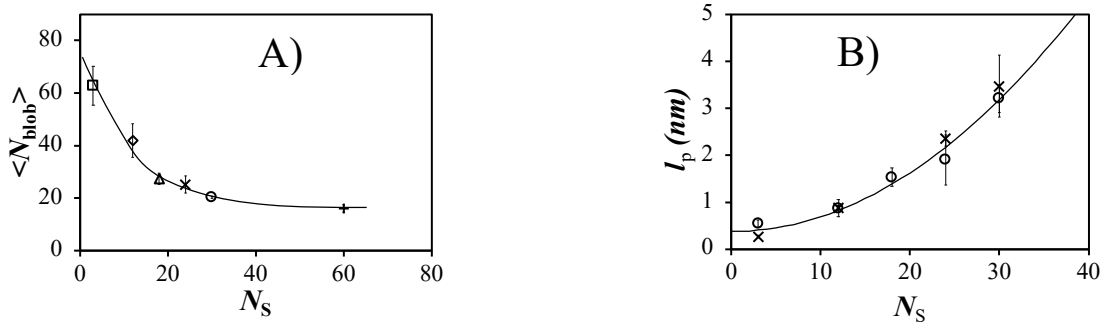

Figure 2. Plot of A) $\langle N_{blob} \rangle$ versus the number of atoms in the sidechain, N_S, and B) l_p versus N_s for the series of Py-PEG$_x$MA calculated by the (○) FBM and (×) GPC analysis in aerated DMSO. (□) PyEG$_5$-PEG$_0$MA, (◇) PyEG$_5$-PEG$_3$MA, (△) PyEG$_5$-PEG$_5$MA, (×) PyEG$_5$-PEG$_7$MA, (○) PyEG$_5$-PEG$_9$MA, and (+) PyEG$_5$-PEG$_{19}$MA.

Py-PEG$_0$MA with the shortest sidechain was the most flexible of all PBBs and adopted a random coil conformation in solution. As a result, it had the largest N_{blob} value of 63 ± 7. Larger N_s values resulted in a stiffening of the main chain as reflected by a decrease in N_{blob} until N_{blob} plateaued for N_s values greater than 30. The plateau region in Figure 2A was attributed to the extended conformation adopted by the Py-PEG$_x$MA samples for large x or N_S values. Since the same EG$_5$ spacer was used to link the pyrenyl label to the polymethacrylate backbone, all Py-PEG$_x$MA samples had the same *blob* size given by $r_{EE,blob}$ in Equation 3. Although $r_{EE,blob}$ took the same value for all Py-PEG$_x$MA samples, the *blobs* were occupied by fewer structural units as N_S increased up to the point where the polymethacrylate backbone was fully extended over the $r_{EE,blob}$ length scale and N_{blob} remained constant and equal to 16 ± 1 for N_S values greater than 30.
The persistence length, l_p, was then calculated using Equation 3 and plotted as a function of N_S in Figure 1B. l_p was found to scale as N_S^2 in Figure 2B as expected for Gaussian side chains.[5] A more quantitative analysis of the l_p-*vs*-N_s trends shown in Figure 1B was achieved by applying Equation 4 which was first introduced by Nakamura and Norisuye.[6] Equation 4 indicates that the stiffness parameter (λ^{-1}) taken as either l_p or the Kuhn length ($l_K = 2 \times l_p$) is the result of two contributions. These contributions to λ^{-1} are the stiffness (λ_o^{-1}) induced by the main polymethacrylate chain and the stiffness (λ_b^{-1}) induced by the excess free energy against bending due to the sidechains.[6] Plotting l_p as a function of N_s^2 in Figure 3A yielded a straight line with a Y-intercept equal to λ_o^{-1}.

$$\lambda^{-1} = \lambda_0^{-1} + \lambda_b^{-1} \tag{4}$$

l_p values calculated using the FBM for Py-PBBs in DMSO were compared to those obtained with a GPC equipped with a viscometer in DMSO (Figure 3A). The excellent agreement found between the l_p values obtained in DMSO by fluorescence and the GPC analysis was taken as validation of the fluorescence study. The l_p calculated for Py-PEG$_{19}$MA from the GPC was found to deviate from the scaling law shown for the shorter side chains. This discrepancy could be attributed to a saturation effect which appears when the side chains, which adopt a random coil conformation, have fully occupied the local volume surrounding the polymethacrylate backbone and prefer to move to a less dense environment perpendicular from the polymer backbone. The break point observed in Figure 3A indicated the point where further increase in N_S would no longer affect l_p.

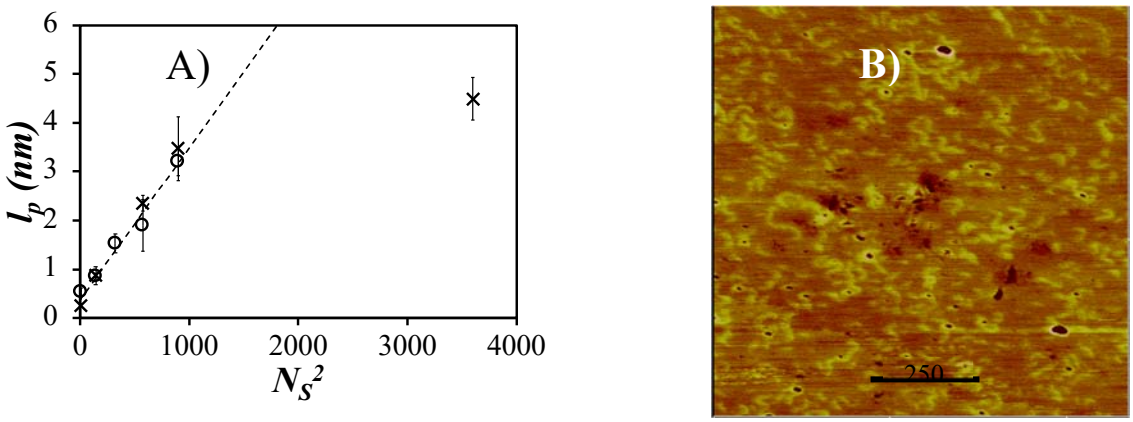

Figure 3. (A) Plot of l_p versus N_s^2 for a series of PEG_xMA calculated from the (○) FBM and (×) GPC analysis. B) AFM height image of $PEG_{19}MA$ on a mica substrate at room temperature.

Finally, atomic force microscopy (AFM) was also used to visualize the $PEG_{19}MA$ sample in Figure 3B. Visual inspection of Figure 3B indicates that the $PEG_{19}MA$ chains are elongated but still flexible thus complementing the results obtained from a combination of PEF and FBM as well as qualitatively agreeing with the l_p of 4.5 nm ± 0.4 nm obtained from GPC analysis.

This study represents the first example in the literature where fluorescence was used to calculate l_p for a series of PBBs with increasing side chain length.

References

(1) Qi, Y.; *et al*. *Nat. Biomed. Eng.* **2016**, *1*, 0002. (2) Mukumoto, K.; *et al*. *Macromolecules* **2014**, *47*, 7852- 7857. (3) Duhamel, J. *Acc. Chem. Res.* **2006**, *39*, 953-960. (4) DeGennes, P-G. Chapter 3 in *Scaling Concepts in Polymer Physics*. Cornell University Press: New York, 1979. pages 69-97. (5) Nakamura Y., Norisuye T. Chapter 5 in *Soft Matter Characterization*, Borsali R., Pecora R. Eds.; Spring Science + Buisness Media, LLC: New York, 2008. pages 277-279. (6) Nakamura, Y.; Norisuye, T. *Polym. J.* **2001,** *33*, 874-878.

Elnaz Esmizadeh
Chemical Engineering
Waterloo

Degradation behavior of polypropylene during reprocessing and its biocomposites: thermal and oxidative degradation kinetics

Degradation behavior of polypropylene during reprocessing and its biocomposites: thermal and oxidative degradation kinetics

Elnaz Esmizadeh, Costas Tzoganakis, and Tizazu H. Mekonnen*
Department of Chemical Engineering, Institute of Polymer Research, University of Waterloo, Waterloo, ON, Canada
*Corresponding Author(s) – E-mail: tmekonnen@uwaterloo.ca

Abstract
Non-isothermal thermogravimetric analysis (TGA) was employed to investigate the degradation of polypropylene (PP) during simulated product manufacturing in a secondary process and wood-plastic composites. Kissinger–Akahira–Sunose (KAS), Ozawa- Flynn-Wall (OFW), Friedman, Kissinger, and Augis models were employed to calculate the apparent activation energy (E_a). Experimental investigation using TGA indicated that the thermograms of PP recyclates shifted to lower temperatures revealing the presence of accelerated degradation process induced by the formation of radicals during chain scission. E_a increased with the extent of degradation (α) and the dependency intensified by reprocessing cycles. In biocomposites, despite the detectable degradation steps of wood and PP in thermal degradation, a partial coincidence of degradation was observed under air.

Keywords: Polypropylene; Recycling; Thermogravimetric analysis; Wood-plastic composites

1. Introduction

Green awareness influences today's industry significantly in several ways to fulfill raising human preference for more eco-friendly procedures and products. Recently, the practice of recycling commodity polymeric materials such as polypropylene (PP) has been encouraged by the ever-growing desire to save resources, reduce the cost, and reuse waste material [1]. Wood-plastic composites (WPC), which typically contain wood (fiber, flour, pulp), plastic, and additives (e.g. coupling agents, processing aids), are substituting plastics, solid wood, and steel in applications such as construction, industrial and agricultural products [2,3]. Various grades of polypropylene[4,5] are extensively utilized as WPC matrices. WPCs can thermally decompose easier with induced degradability due to the inherent low thermal stability of wood-based reinforcements, desired for reducing environmental disadvantage [6]. However, the degradation of wood components during the thermo-mechanical processing of WPCs may lead to several undesirable properties in the fabricated products, such as deterioration of color, unpleasant odor, and poor mechanical properties[5,7].

The knowledge of degradation origins and kinetics both in oxidative and non-oxidative is of fundamental importance to determine the lifespan of the product, the effective conditions of processing, and how to control unfavorable degradation[8]. Thus, the objective of this work was to investigate the thermal and oxidative degradation kinetics using the various models. An internal batch mixer was employed to simulate recycling to avoid oxidation further.

2. Materials and Methods

Polypropylene homopolymer powder (Pro-fax 6301) and Maple wood flour (mesh 600) from LyondellBasell (USA) and Ontario Sawdust Supplies (Canada), respectively, were used in this study. The composition of the WPCs was shown by $PP^{\times n \text{ or } v}\ W_x$, where v is virgin, $\times$n is n-time processed and x is 40 or 60 (wt.% of wood). The materials were compounded in a HAAKE Rheomix 3000 batch mixer at the mixing temperature of 180°C and rotor speed of 80rpm. Thermogravimetric analyses (TGA) were performed on a TA instrument Q500 analyzer both under nitrogen and air atmosphere with a 40 ml/min flow, respectively.

3. Results and discussion

3.1. Effect of reprocessing cycles

Figure 1 shows the thermogravimetric (TG) and the first-order derivative (DTG) curves at a heating rate of β=5 ºC/min and 20 ºC/min of the virgin PP and the samples reprocessed by batch mixing under non-oxidative and oxidative environment. As expected, increasing the heating rate led to a shift of the thermograms towards higher temperatures both in oxidative and non-oxidative degradation. This is due to the shorter retention time at the higher heating rates which limit time-consuming molecular motions taking place before decomposition [9]. All curves exhibit one-step degradation that can be attributed to the radical random scission commonly occurring with the thermal degradation of the polyolefins [10]. In a nitrogen environment, PP degrades in a single step beginning at 300 ºC and ending at 475 ºC. On the other hand, it degrades from about 250 to 425 ºC primarily in a single step in the presence of air. Under both environments, all PP samples have degraded completely without leaving any significant residue. It can also evidently be observed that the thermo-oxidative decomposition took place at lower temperatures compared with the inert environment. Besides, the degradative effect of reprocessing cycles is more pronounced in the experiments under the air.

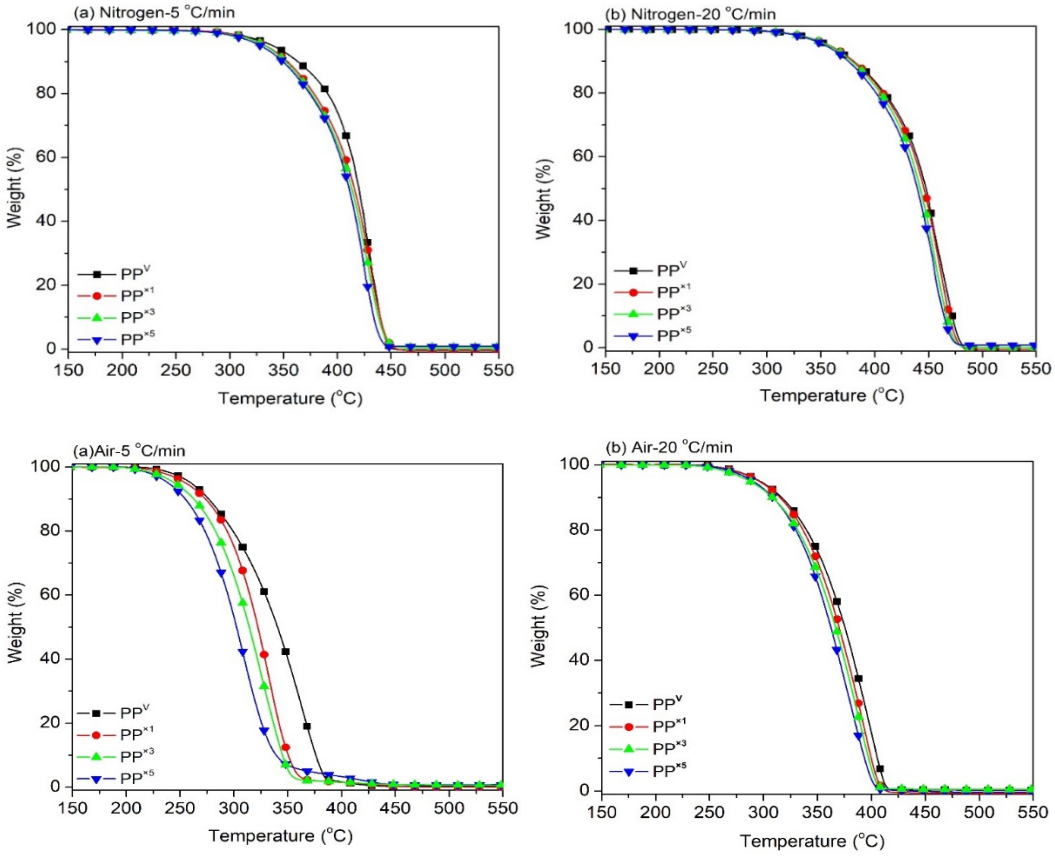

Figure 1. TG curves for the effect of reprocessing cycles on the thermal/oxidative decomposition of PP

The activation energy (E_a) values versus α for virgin PP and its recyclates decomposed under N_2 and the air calculated from various models were demonstrated in Figure 2. A gradual increase in E_a values with an increase in the degree of conversion was observed for all the samples. Lower E_a values at early stages of degradation suggest that at low conversions decomposition, kinetics was limited by initiation at the weak links. The increasing trend with the evolution of E_a can be

interpreted by a shift in the rate-limiting step from initiation at the weak links to the degradation initiated by random scission [11].

3.2. Effect of wood

TGA/DTG curves of the wood fiber and PP-based WPCs in nitrogen and air atmospheres are presented in Figure 3. Three distinct stages were for the thermal degradation of the well-dried wood fiber under a nitrogen atmosphere. In the beginning, a small step degradation occurred below 100 ºC; followed by a second step that occurred at 220-315 ºC and the last one occurred at 315-400 ºC which can be related to the volatilization of the wood extractives; the decomposition of the hemicelluloses; and the decomposition of cellulose, respectively [6,12,13].

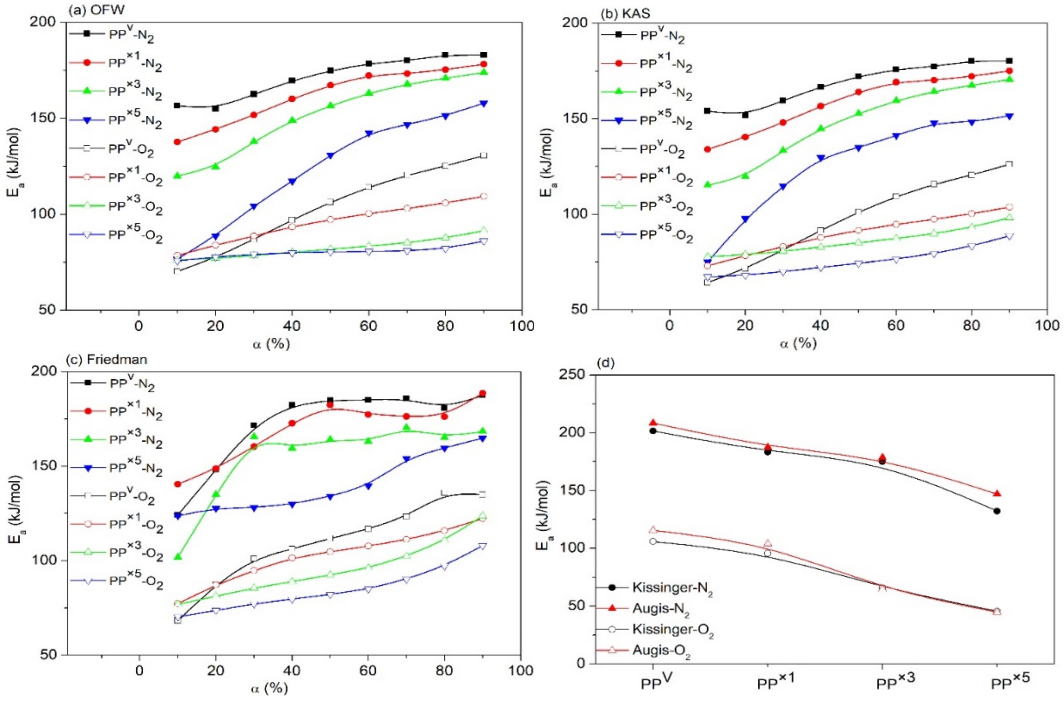

Figure 2. Activation energies (E_a) for virgin PP and its recyclates obtained by different models

The other main component of wood fiber, lignin is the most stable component to thermal decomposition without any specific peak. However, in the case of oxidative degradation, a small peak that occurred at 400-500 ºC, which can be related to the degradation of lignin. A clear indication is that in the WPC systems, the degradation of the two components can be easily detected individually owing to the noticeable difference in their thermal stability. A slight rightward shift in the degradation peak temperature of cellulose and PP is observed in the case of WPCs. Under the exposure of PP-based WPC to the air atmosphere, the oxidative degradation of all components commences sooner as compared to the nitrogen atmosphere. Interestingly, T_{onset} and T_{peak} of wood and PP^vW00 become close to each other in the presence of oxygen. Narrow temperature interval between the occurrence of oxidative degradation of wood fiber and PP is attributed to the partial co-occurance of their degradation in a wide temperature range. At the heating rate of 5 ºC/min, the degradation profile of WPC did not fall between PP and wood fiber curves, but by increasing the heating rate, the curves gradually move toward the area between the two components. At the low heating rate, the volatile compounds evolved in oxidative degradation

of wood fiber reduce access of oxygen species to the polymer chains. With the lack of access to oxygen, PP requires a higher temperature to decompose than normal oxidative degradation.

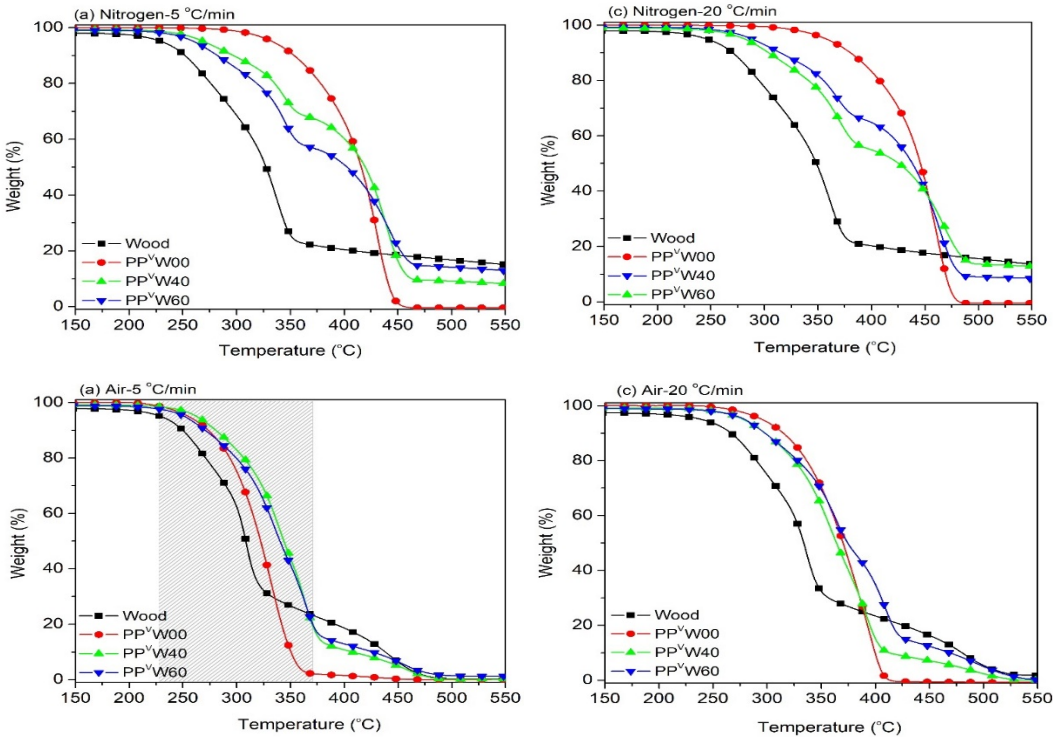

Figure 3. Thermal/oxidative degradation of wood fiber and PP-based WPCs

To analysis the effect of wood on the degradation of PP precisely, the DTG curves were deconvoluted to separate the overlapped cellulose and PP peak. The values of the deconvoluted figures were employed to determine E_a proposed by iso-conversional models. For instance, the plots of the FWO method, which was employed for the calculation of the E_a values for PP deconvoluted from WPCs are illustrated in Figure 4. Under an inert environment, the shape of the E_a evolution curves for PP degradation deconvoluted from WPCs was similar to PP sample without wood (PP^VW00). Under the air, however, the E_a evolution curve of PP deconvoluted from WPCs showed an irregular decreasing trend with the conversion.

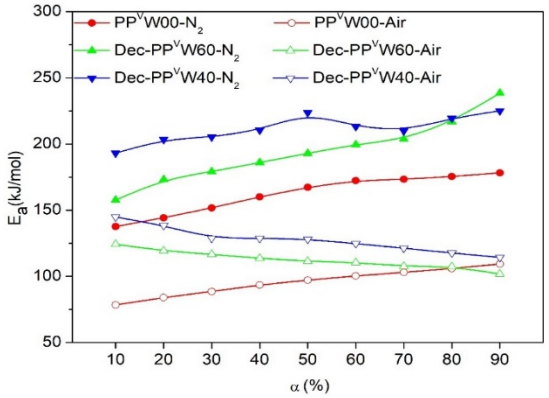

Figure 4. Variation of E_a for individual PP degradation obtained from deconvolution WPCs (OFW model)

4. Conclusions

The degradation behavior of a simulated recycled PP and wood-PP biocomposites have been analyzed by TGA. Three iso-conversional methods, KAS, OFW, and Friedman, and two conversion-independent methods, Kissinger and Augis were employed to calculate E_a. T_{onset} and T_{peak} reduction. The results revealed that the PP underwent substantial degradation after reprocessing, confirmed by a remarkable drop of τ_∞ accompanied by an increase in MFR. A progressive reduction was observed for E_a with the successive reprocessing cycles at a whole range of conversion.

In the WPC systems, two probable mechanisms, heat sink effect of the residual ash and thermal insulating effect of the foam-like structure of PP were proposed to cause a slight increase in T_{peak} of PP during thermal degradation. An interesting observation in the oxidation of WPCs was that the TGA profile did not fall between PP and wood curves, at low heating rates. The reduction in oxygen access by the polymer chains due to the evolved volatile compounds from wood was the most probable reason for this. Overlapping tails of degradation peaks corresponding to cellulose and PP was observed for degradation of WPCs. The Lorentzian area deconvolution method employed to separate them indicated that under N_2, the E_a evolution curves for PP shifted upward at the whole range of conversion due to thermal absorbency of the residual chars. Under the air, a significant increase in E_a values was observed at the initial steps of degradation, which was associated with the high volume of degradation volatiles generated from wood that reduced the oxygen diffusion. At high conversions, the effect of wood became negligible as there was no residual remained from the decomposition of wood.

Acknowledgments

We gratefully acknowledge financial support from Natural Resources Canada (NRCan) for this research work. We are grateful to Ontario Sawdust Supplies for the supply of wood fiber.

References

[1] S.M. Al-Salem, P. Lettieri, J. Baeyens, Waste Manag. 29 (2009) 2625–2643.
[2] D.W. Thompson, E.N. Hansen, C. Knowles, L. Muszynski, 5 (2010) 1336–1552.
[3] A. Ashori, Bioresour. Technol. 99 (2008) 4661–4667.
[4] M. Sain, P. Suhara, S. Law, A. Bouilloux, J. Reinf. Plast. Compos. 24 (2005) 121–130.
[5] M. Tajvidi, A. Takemura, J. Thermoplast. Compos. Mater. 23 (2010) 281–298.
[6] M. Poletto, J. Dettenborn, V. Pistor, M. Zeni, A.J. Zattera, Mater. Res. 13 (2010) 375–379.
[7] A. Awal, S. Ghosh, M. Sain, J. Therm. Anal. Calorim. 99 (2009) 695–701.
[8] J. Aurrekoetxea, M.A. Sarrionandia, I. Urrutibeascoa, M.L. Maspoch, J. Mater. Sci. 36 (2001) 2607–2613.
[9] K. Selim, S. Özkar, L. Yilmaz, J. Appl. Polym. Sci. 77 (2000) 538–546.
[10] K. Wang, F. Addiego, N. Bahlouli, S. Ahzi, Y. Rémond, V. Toniazzo, R. Muller, Polym. Degrad. Stab. 97 (2012) 1475–1484.
[11] J.D. Peterson, S. Vyazovkin, C.A. Wight, Macromol. Chem. Phys. 202 (2001) 775–784.
[12] T.R. Rao, A. Sharma, Energy. 23 (1998) 973–978.
[13] H. Yang, R. Yan, H. Chen, D.H. Lee, C. Zheng, Fuel. 86 (2007) 1781–1788.

Sainiwetha Saihrishnan
Chemical Engineering
Waterloo

Thermo-mechanical Degradation of Polypropylene-Low Density Polyethylene blend system after multiple extrusion

Thermo-mechanical Degradation of PP/LDPE Blends Exposed to Simulated Recycling

Prof. Tizazu Mekonnen
Prof. Costas Tzoganakis

Sainiwetha Saikrishnan
MASc, Chemical Engineering

Institute for Polymer Research
IPR
University of Waterloo

UNIVERSITY OF WATERLOO | FACULTY OF ENGINEERING

Contents

UNIVERSITY OF WATERLOO | FACULTY OF ENGINEERING

Introduction

- Since the 1950s, global production or conversion of resin has grown 8% from 28 million tonnes (Mt) to 359 Mt in 2018
- Main sectors of plastic production and waste generation: packaging, construction and transportation
- Important to understand the magnitude and mechanisms of property deterioration during the recycling process while, looking into possible utilizations, applications, and solutions for the existing global accumulated polyolefin waste

Different types plastics in various application

UNIVERSITY OF WATERLOO | FACULTY OF ENGINEERING

Experiment & Results

- Extrusion: Twin screw extruder – 120 °C - 200 °C
- Injection molding and compression molding
- Parallel plate rheometry, Capillary rheometry, TGA, DSC, MFI, Tensile properties, FTIR, Optical microscopy

- The viscosity of the samples decreased as the reprocessing cycle increased from 1 to 5, except for the LDPE sample (0/100)
- The shift in viscosity from a higher modulus to a lower modulus was likely attributed to the decrease in molecular weight as a result of the shear and temperature exposure during recycling

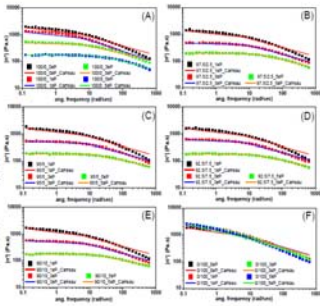

UNIVERSITY OF WATERLOO | FACULTY OF ENGINEERING

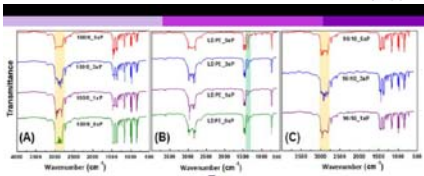

- The peak observed (PP, Figure (A)) between 1386 – 1353 cm^{-1} and 1477 – 1432 cm^{-1} was due to methyl group vibrations
- A progressive increase in the intensity of a small transmission band at ~ 1370 cm^{-1} was noted with the increase in the re-processing cycle from zero to five-time reprocessing of LDPE

- **Melt flow rate:**
- The formulated blends and neat PP have shown an increase in MFR as the processing cycle increased from 1 to 5 as shown in the figure (bottom right corner)
- LDPE does not show significant change in MFI

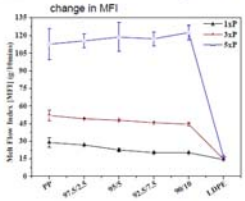

UNIVERSITY OF WATERLOO | FACULTY OF ENGINEERING

Conclusion

- Why recycle: to reduce plastic pollution, moving towards circular economy
- Recycling: chemical, mechanical and energy recovery
- As processing count increases – MFI increases, viscosity decreases – Molecular weight also decreases (from Literature)
- TGA analysis and FTIR also supported that pure PP and PP/LDPE blends undergo thermo-mechanical degradation due to chain scission and formation of smaller molecules.
- This study showed that low concentrations of LDPE in PP does not affect the system and the characteristics of PP dominates. It can also be concluded that property deterioration in all the samples is not that significant even after five extrusion cycles

Recommendations

- Investigation of the change in the molecular weight, environmental stress crack analysis, color analysis, and impact strength.
- Increasing the reprocessing cycle number beyond 5 cycles (e.g. for up to 10 cycles) and analyzing the change in properties
- Increasing the amount of LDPE in the blend system provides useful information and broader understanding of the reprocessibility and change in structure – property of PP/LDPE blend systems.
- Reducing plastic pollution by efficient usage of plastics and reusing the existing plastics

UNIVERSITY OF WATERLOO | FACULTY OF ENGINEERING

Javan Buratynski
Chemistry
Waterloo

Using Degradable Polymers to Separate Carbon Nanotubes

Separation of Carbon Nanotubes Using Degradable Polymers

Javan Buratynski

September 2nd, 2020

Supervisor: Dr. Derek Schipper

Polymer Wrapping

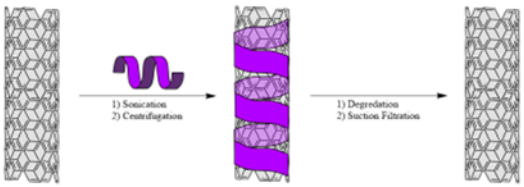

- Important aspects for polymers:
  - Selectively separate carbon nanotube chiralities
  - Synthetically simple
  - Mild degradation conditions

Target Polymer Backbone

- Target polymer synthesised through direct arylation
- Degraded using *m*CPBA

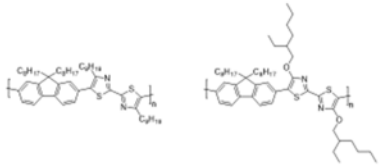

Preliminary Results

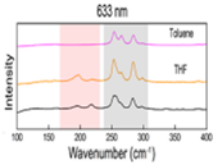

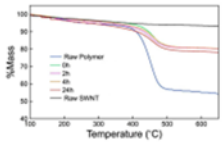

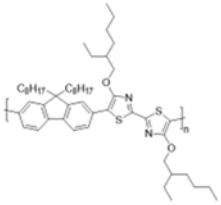

Figures Provided by James Bodnaryk of the Adronov Group

Summary

- Carbon nanotubes could play a large role as in a variety of fields as long as they can be separated
- Our polymer presents an effective separation method with breakdown possibly allowing for separation and retrieval of target SWNTs

Acknowledgments

- The Schipper Group:
  - Geoff Sinclair
  - Rafael Mirabal
  - Jianan Wang
  - Sarah Mathers
  - Serxho Selmani
  - Rob Claridge
- Supervisor:
  - Dr. Derek Schipper
- The Adronov Group
  - James Bodnarynk

Institute for Polymer Research
IPR
University of Waterloo

Abdullah Ba Salem
Chemistry
Waterloo

Determination of Aggregation Number for Pyrene-labeled Gemini Surfactants

UNIVERSITY OF WATERLOO

Determination of the Aggregation Number for Pyrene-Labeled Gemini Surfactants by Fluorescence Quenching

Abdullah Basalem
Supervisor: Jean Duhamel

Sep. 2020

Gemini Surfactants

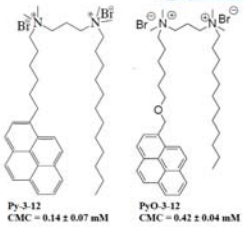

- More than one fold of magnitude lower CMC than its regular counterparts.
- Promising as gene transfection vehicles.
- Characterization of these surfactants (CMC & N_{agg}).

Zana, R., & Xia, J. (2004). Gemini surfactants: Synthesis, interfacial and solution-phase behavior, and applications. New York: Marcel Dekker.

N_{agg} Determination by Quenching

$$P_m = \frac{< n >^m}{m!} e^{-<n>}$$

$$< n > = \frac{[Q]_{bound}}{[Micelle]}$$

$$\boxed{< n > = \frac{N_{agg}}{[Surfactant] - CMC}[Q]_{bound}}$$

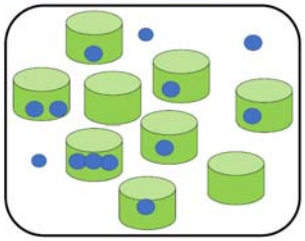

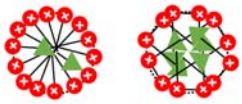

N_{agg} Determination by Quenching

$$\boxed{< n > = \frac{N_{agg}}{[Surfactant] - CMC}[Q]_{bound}}$$

$$[Q]_{bound} = [Q]_{total} - [Q]_{free}$$

$$\frac{I_o}{I} = \frac{\tau_o}{\tau} = 1 + k_q \tau_o [Q]_{free}$$

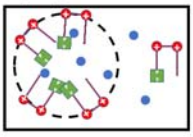

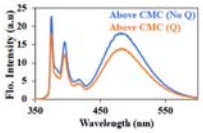

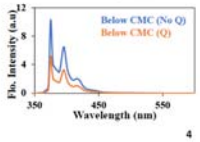

J. Chem. Educ. **1995** *72*, 662-663.

N_{agg} Determination by Quenching

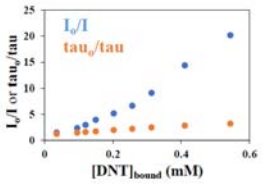

$$\frac{I_o}{I} = SQ \times DQ$$

$$\frac{I_o}{I} = (1 + K_S[Q])\,(1 + k D \tau_o [Q])$$

$$\frac{\tau_o}{\tau} = 1 + k D \tau_o [Q]$$

At low [Q]:

$$e^{[Q]/[Sphere\ of\ Action]} = e^{[Q]/[micelle]} = 1 + KS[Q]$$

$$\frac{\frac{I_o}{I}}{\frac{\tau_o}{\tau}} = 1 + KS[Q] = e^{<N>}$$

$$\ln \frac{\frac{I_o}{I}}{\frac{\tau_o}{\tau}} = < n >_S$$

Conclusions & Acknowledgments

- Prof. Jean Duhamel
- Duhamel lab members
- NSERC & HEHD

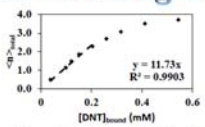

- The CMC for both gemini surfactants Py-3-12 and PyO-3-12 was found to be 0.14 ± 0.07 mM and 0.42 ± 0.04 mM respectively.
- N_{agg} was found to be 22 ± 0.5 units for Py-3-12 and 20 ± 1 units for PyO-3-12.

UNIVERSITY OF WATERLOO

NSERC CRSNG

Kristijan Lulic
Chemistry
Waterloo

Self-Association of Oligoquinoline Foldamers Probed by Fluorescence Anisotropy

Self-Association of Oligoquinoline Foldamers Probed by Fluorescence Anisotropy

By: Kristijan Lulic
Supervisor: Jean Duhamel

UNIVERSITY OF WATERLOO | FACULTY OF SCIENCE

Institute for Polymer Research IPR University of Waterloo

Foldamers and Molecular Wires

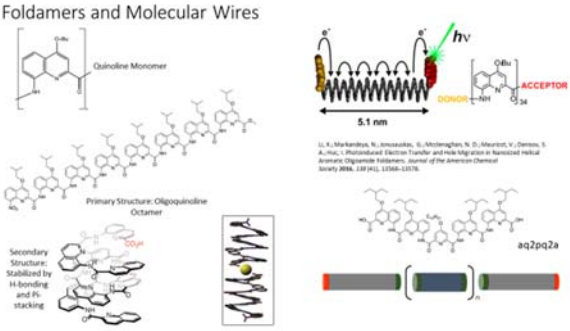

Time-Resolved Fluorescence Anisotropy (TRFA) for Equilibrium Studies

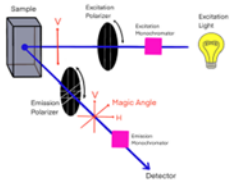

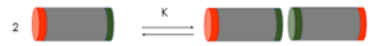

$$[A] = \frac{-1 + \sqrt{1 + 8K[A]_o}}{4K} \qquad [A_2] = \frac{1 + 4K[A]_o - \sqrt{1 + 8K[A]_o}}{8K}$$

$$< \phi > = \frac{[A]\phi_1 + 2[A_2]\phi_2}{[A]_o}$$

$$\phi = \frac{\eta V_h}{RT}$$

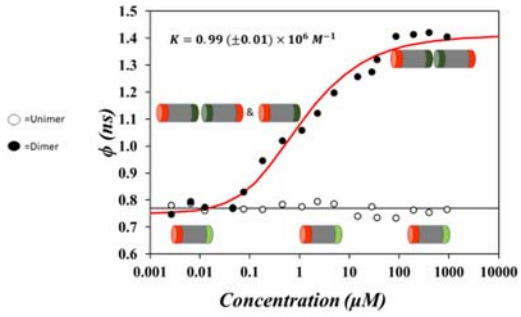

Acknowledgements

- Dr.Jean Duhamel
- Lab Members of the Duhamel Group
- Dr. Huc's Group for foldamer samples
  - Jingqi Wang

université de BORDEAUX

Institute for Polymer Research IPR University of Waterloo

Hunter Little
Chemistry
Waterloo

Progress in Instrumentation for Time-resolved Fluorescence Anisotropy

Progress in Instrumentation for Time-resolved Fluorescence Anisotropy

Hunter Little
Duhamel Group
September 2, 2020

UNIVERSITY OF WATERLOO
FACULTY OF SCIENCE

1

Fluorescence Anisotropy

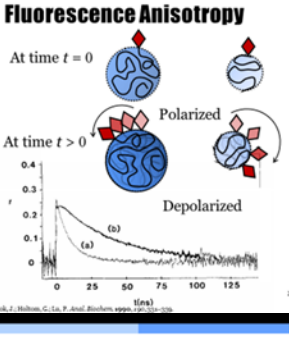

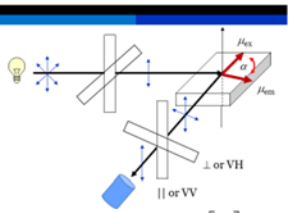

$$r(t) = \frac{I_{VV}(t) - G \times I_{VH}(t)}{I_{VV}(t) + G \times 2 \times I_{VH}(t)} = r_o \exp\left[\frac{-t}{\phi}\right]$$

$$\phi = \frac{\eta}{RT} V_h$$

Cook, J.; Holtom, G.; Lu, P. *Anal. Biochem.* **1990**, *190*, 359–376.

2

Analysis Methods

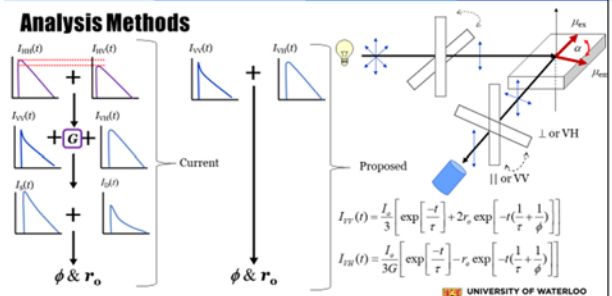

$$I_{VV}(t) = \frac{I_{\parallel}}{3}\left[\exp\left[\frac{-t}{\tau}\right] + 2r_o \exp\left[-t\left(\frac{1}{\tau} + \frac{1}{\phi}\right)\right]\right]$$

$$I_{VH}(t) = \frac{I_{\perp}}{3G}\left[\exp\left[\frac{-t}{\tau}\right] - r_o \exp\left[-t\left(\frac{1}{\tau} + \frac{1}{\phi}\right)\right]\right]$$

Lakowicz, J. R., *Principles of Fluorescence Spectroscopy* (3rd ed.). New York: Springer Science **2006**, 353 – 402
Green, A. J.; Fleming, G. R. *Biophys J.* **1983**, *36* (1), 45–56.
Dale, R. E.; Chen, L. A.; Brand, L. *J. Biol. Chem.* **1977**, *252* (21), 7500–7510

3

Recent Advancements

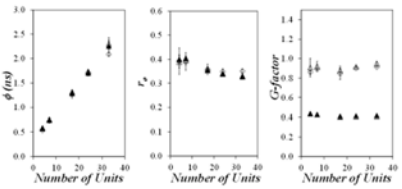

(◇) Conventional Analysis , Global Analysis with (△) toggling and (▲) static polarizers

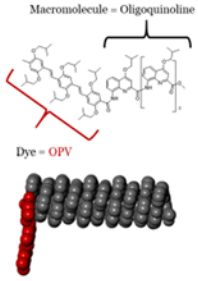

Little, H.; Wang, J.; Duhamel, J.; Li, X.; Markandeya, N.; Maurizot, V.; Huc, I. Simplification in the Acquisition and Analysis of Fluorescence Decays Acquired with Polarized Emission for Time-Resolved Fluorescence Anisotropy Measurements. *Anal. Chem.* **2020**, *92*, 668–673.

4

Conclusions

- Optimizing the *G*-factor yields the same experimental results as when it is determined via a cumbersome and expensive experimental set up

Current	Proposed
6 Decays in Analysis	2 Decays in Analysis
Automated Polarizers	**Standard Polarizers**
Specialized Electronics	**Standard Electronics**
Calculated *G*-factor	Optimized *G*-factor
Same ϕ value	
Same r_o value	

Acknowledgments

- Prof. Jean Duhamel
- Jingqi Wang, Kristijan Lulic, Harmoit Singh Bindra
- Members of the Duhamel & Huc Groups

NSERC CRSNG
Institute for Polymer Research IPR University of Waterloo
université de BORDEAUX

5

Franklin Frasca
Chemistry
Waterloo

Relating Pyrene Excimer Fluorescence to Conformation in Pyrene-Labeled Polyamines

Relating Pyrene Excimer Fluorescence to Conformation in Pyrene-Labeled Polyamines

By: Franklin Frasca
Supervisor: Jean Duhamel

University of Waterloo

Afton CHEMICAL

Institute for Polymer Research
IPR
University of Waterloo

1

Background – Fluorescence of Pyrene

$$[Py]_{loc} = \frac{\#\ of\ G.S.\ Pyrenes}{\frac{4}{3}\pi\left(\frac{\langle L_{Py}^2\rangle^{1/2}}{2}\right)^3}$$

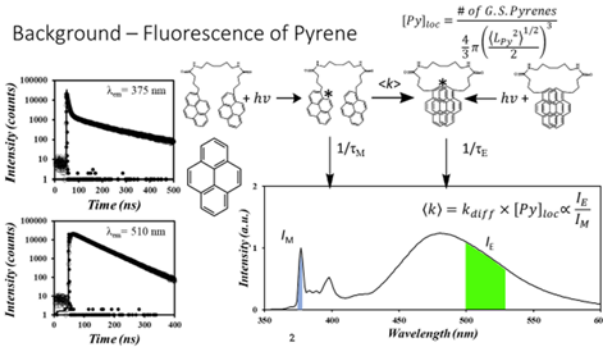

2

A series of pyrene-labeled polyamines is being prepared to assess how both the I_E/I_M ratio and <k> scale with increasing $[Py]_{loc}$.

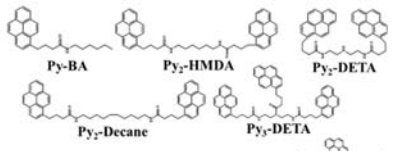

Product	$[Py]_{loc}$ ($Å^{-3}$)	I_E/I_M
Py_2-Decane	0.011	4.4
Py_2-HMDA	0.015	8.2
Py_2-DETA	0.017	10.9
Py_3-DETA	0.042	31.6

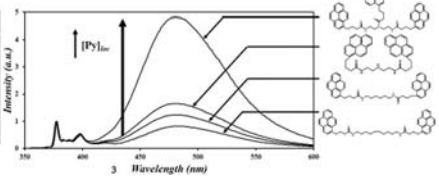

3

Relating <k> to $[Py]_{loc}$

$$\langle k \rangle = k_{diff} \times [Py]_{loc} \propto \frac{I_E}{I_M}$$

$$[Py]_{loc} = \frac{\#\ of\ G.S.\ Pyrenes}{\frac{4}{3}\pi\left(\frac{\langle L_{Py}^2\rangle^{1/2}}{2}\right)^3}$$

Ex:

$\langle L_{Py}^2\rangle^{1/2} = \sqrt{16} \times 1.25\ Å = 5\ Å$

$\rightarrow [Py]_{loc} = 0.015\ Å^{-3}$

Product	$[Py]_{loc}$ ($Å^{-3}$)	<k> (ns^{-1})
Py_2-Decane	0.011	0.039
Py_2-HMDA	0.015	0.083
Py_2-DETA	0.017	0.098
Py_3-DETA	0.042	0.210

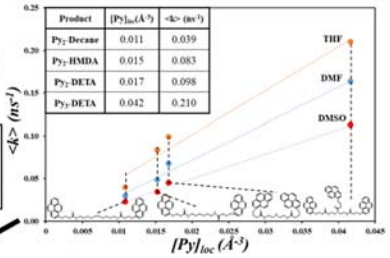

4

Conclusions

Since the rate constant <k> for pyrene excimer formation of the pyrene-labeled polyamines is directly proportional to the local concentration of pyrene, the linear relationship between <k> and $[Py]_{loc}$ suggest that the expression for $[Py]_{loc}$, which was derived in an earlier publication [1], is valid.

Thus, <k> can be used to assess the local amine concentration experienced in a polyamine by covalently labeling the polyamine with the appropriate pyrene derivative.

Acknowledgements

- Afton Chemical
- Duhamel Group Members

[1] McNelles, S.; Thoma, J.; Adronov, A.; Duhamel, J. Quantitative Characterization of the Molecular Dimensions of Flexible Dendritic Macromolecules by Pyrene Excimer Fluorescence. *Macromolecules* **2018**, *51*, 1586-1590

Afton CHEMICAL

University of Waterloo

Institute for Polymer Research
IPR
University of Waterloo

Tiana Trumpur
Physics and Astronomy
Waterloo

Solvent Induced Nanoscopic Roughness on Glassy Polymer Thin Films

Solvent Induced Nanoscopic Roughness on Glassy Polymer Thin Films

2020 IPR Symposium

Tiana Trumpour, Adam Reagen, James Forrest

Department of Physics, University of Waterloo, Canada
Perimeter Institute for Theoretical Physics, Waterloo, Canada

September 2nd, 2020

Introduction & Background

Solvents

→ *Good solvents completely dissolve the polymer thin film (eg. Toluene for PS)*
→ *Poor solvents have no "lasting" effect on the surface (eg. Pentane for PS)*

Previous work completed in this field
→ *Karim et al. 1998*
→ *Strawhecker et al. 2001*
→ *Statt et al. 2017*

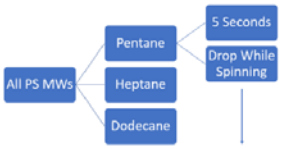

Experimental Morphology

Surface morphology measured by atomic force microscopy and radial power spectral density function (PSDF)

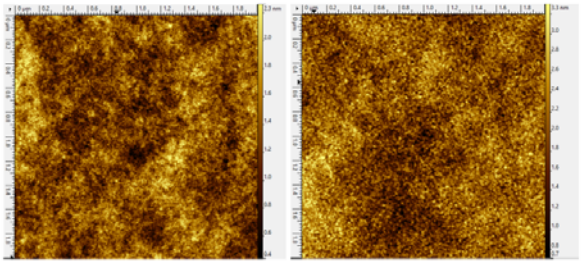

Figure: Untreated Film

Figure: Treated Film

Results

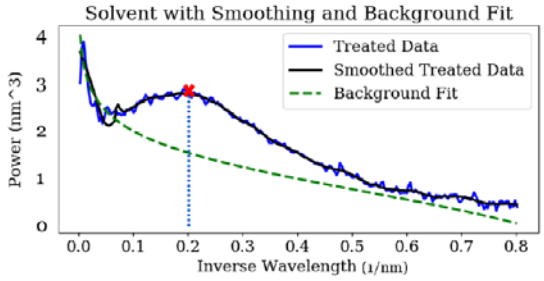

Results

Characteristic length scales ranging from 25-165 nm

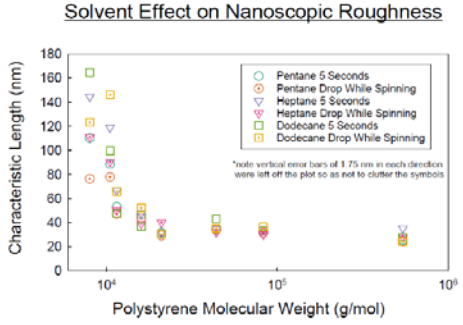

Conclusions

Poor solvents produce a nanoscopic surface morphology with a characteristic length scale
→ *Independent of solvent type or exposure time*

Similar results seen with other glass-forming polymers (eg. PMMA)

Implications

Morphology on scale of nanolithography leading to major surface instability for small scale electronics and other technologies

Minghui Liu
Chemical Engineering
Waterloo

Antimicrobial Activity of Quaternary Ammonium Compound/Polyurethane [QAC/PU] Colloidal Complex Film Based on Synergetic Release Killing and Contact Killing Mechanisms

Antimicrobial activity of quaternary ammonium compound/polyurethane (QAC/PU) colloidal complex film based on synergetic release killing and contact killing mechanisms

8/18/2020

Presented by: Minghui Liu 20813284
Supervisor: Boxin Zhao

UNIVERSITY OF WATERLOO | FACULTY OF ENGINEERING

Synthesis of QAC/PU colloidal complex film

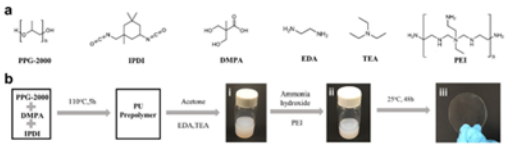

Isophorone diisocyanate (IPDI); polypropylene glycol-2000 (PPG-2000); dimethylolpropanic acid (DMPA); Ethylenediamine (EDA); Triethylamine (TEA); branched polyethyleneimine (PEI) (average Mw ~25000)

QAC/PU colloidal complex film network

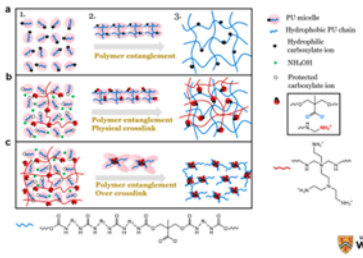

Antibacterial mechanism- QACs molecules

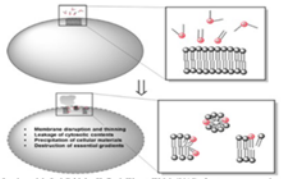

Jennings, M. C., Minbiole, K. P., & Wuest, W. M. (2015). Quaternary ammonium compounds: an antimicrobial mainstay and platform for innovation to address bacterial resistance. *ACS infectious diseases*, *1*(7), 288-303.

1. QAC molecules (+) cell surface (-) QAC molecules replace ions from cytoplasmic membrane- destabilize the intracellular of the bacterium.
2. hydrophobicity-leakage of intracellular fluid.

PAGE 4

Antibacterial test – release-killing

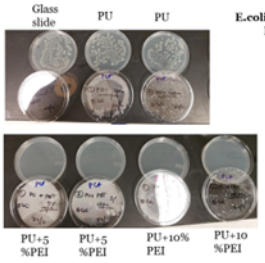

E.coli colonies cultured after contact with glass slide, PU, PU+5wt%PEI and PU+10wt%PEI for 1h

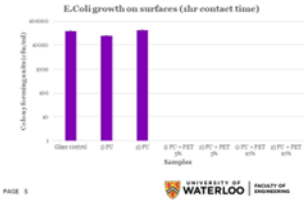

PAGE 5

QACs Leaching test of QAC/PU colloidal systems by conductivity

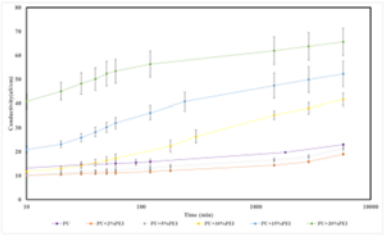

PRESENTATION TITLE

PAGE 6

Remi Casier
Chemistry
Waterloo

Copolymerization and its Effects on Polymer Dynamics in Solution

Copolymerization and its Effects on Polymer Dynamics in Solution

Remi Casier and Jean Duhamel

INTRODUCTION

The bulk properties of polymers are typically described by their glass transition temperature (T_g). The effect that copolymerization has on T_g has been extensively studied leading to several commonly used equations, such as the Fox[1] and Gordon-Taylor-Wood[2,3] equations, which are able to predict the T_g of copolymers based on their comonomer constituents.[4] Despite this, little has been done to study how copolymerization affects the dynamics of polymers in solution in a controlled manner. The solution dynamics of polymers are not only important to the ability of macromolecules to spontaneously form ordered structures in solution[5] but also plays an important role in the rheological properties of polymer solutions.[6] The goal of this study is to help answer two questions: How does the structure (size) and content of each comonomer affect the dynamics of the resulting copolymer in solution. To this end, a series of copolypeptides were prepared with amino acids of varying size. By studying how the internal dynamics of the copolypeptides responded to changes in comonomer size and level of incorporation, the copolypeptides could be viewed as model systems to probe the solution behaviour of copolymers in a controlled setting.

EXPERIMENTAL

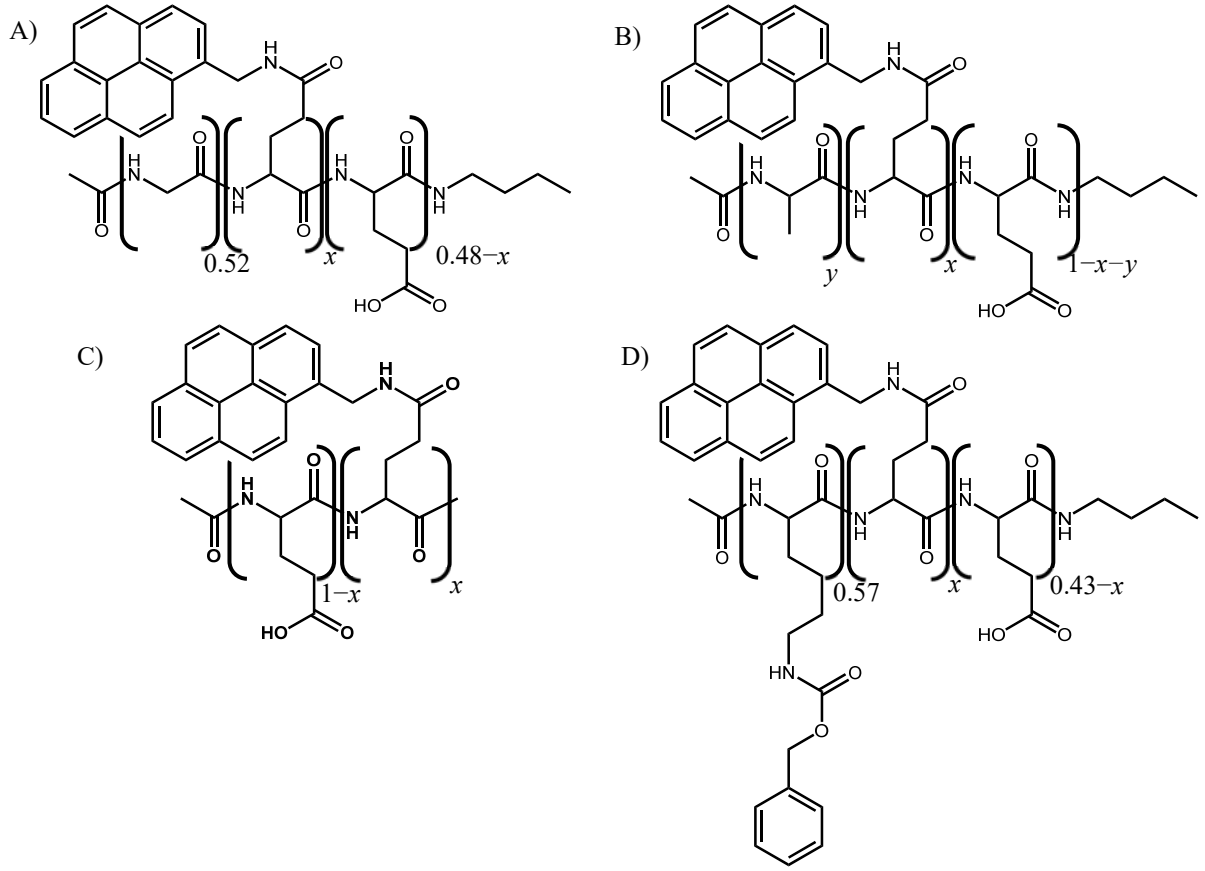

Figure 1. The chemical structures of pyrene-labeled A) poly(glycine-*co*-*D*,*L*-glutamic acid) (Py-PGlyGA), B) poly(*D*,*L*-alanine-*co*-*D*,*L*-glutamic acid) (Py-PAlaGA), C) poly(*D*,*L*-glutamic acid) (Py-PGA), and D) poly(carboxybenzyl-protected *D*,*L*-lysine-*co*-*D*,*L*-glutamic acid) (Py-PLys(Z)GA). All stereocenters in the chemical structures are racemic.

Copolypeptides were prepared via a ring-opening polymerization of the *D*,*L*-*N*-carboxyanhydride (NCA) derivatives of *t*-butyl-protected glutamic acid (GA) with glycine (Gly), alanine (Ala), or carboxybenzyl-protected lysine (Lys(Z)). The *D,L*-isomers of all the amino acids were used to prevent the polypeptides from forming secondary structures (ex. α-helices) in solution, thus ensuring they all adopted a random-coil conformation. After deprotecting the GA's with trifluoroacetic acid, a molar fraction x of the structural units was labeled with 1-pyrenemethylamine. Each polypeptide was prepared with several pyrene contents. The structures of the pyrene-labeled polypeptides used in this study are given in Figure 1.

The copolypeptides were characterized by ^{1}H NMR and GPC to determine their structural unit composition and absolute molecular weights, respectively. Their pyrene contents were determined by UV-Vis absorption measurements. A summary of the parameters describing the pyrene-labeled polypeptides is given in Table 1. The pyrene-labeled polypeptides were characterized by steady-state and time-resolved fluorescence. The monomer and excimer time-resolved fluorescence decays were globally analyzed with the fluorescence *blob* model (FBM). Briefly, the FBM divides a macromolecule into a series of homogeneous subvolumes (*blobs*). The FBM analysis of the fluorescence decays yielded N_{blob}, the number of structural units inside a *blob*, and k_{blob}, the rate constant at which those structural units encountered one another inside a *blob*. Although the *blob* volume was expected to be the same for all the polypeptides used in this study, the N_{blob} values could be different. Therefore the product $k_{blob}\times N_{blob}$ provided a better description of the polypeptide dynamics, as this product represents the number of diffusive encounters between the structural units per unit time in a *blob*.

Table 1: The composition, pyrene contents (x), number-average molecular weight (M_n), degree of polymerization (DP), and dispersity ($Đ$) of the polypeptides shown in Figure 1.

Polypeptide	***Polypeptide Composition***		**# Py labelings**	***x* (mol%)**	***M*$_n$ (kg·mol^{-1})**	***DP***	***Đ***
	mol% GA	mol% comonomer					
PGlyGA	48	4	4	3.5–5.3	13	150	-
PAlaGA	42	4	4	6.6–15.2	23	240	1.05
	59	5	5	6.6–10.4	16	150	1.21
	76	5	5	3.3–5.0	10	90	1.10
PGA	100	5	5	6.0–12.3	100	784	1.07
PLys(Z)GA	43	5	5	4.5–13.2	37	180	1.04

RESULTS AND DISCUSSION

In order to probe the effects of copolymerization on the internal dynamics of polypeptides, a series of copolypeptides (Figure 1) were prepared such that each contained glutamic acid (GA) while the comonomer was varied. In this manner the effect that each of the comonomers had on the dynamics of a poly(glutamic acid) (PGA) base polymer could be studied in a systematic manner. To quantify the differences between each of the chosen comonomers, each comonomer was assigned a value based on the number of non-hydrogen atoms in their side chains. This so-called *side chain size* (*SCS*) equaled 0 for Gly, 1 for Ala, 5 for Gly, and 15 for Lys(Z).

Comonomer Side Chain Size: To determine what effect comonomer size has on the internal structure and dynamics of polypeptides, a set of the polypeptides in Figure 1 were prepared such that each of them contained a similar amount of comonomer (ca. 44 (±3) mol%). This ensured that any observed differences between them must have originated from changes in the comonomer size

and was not due to changes in composition. For each polypeptide, the N_{blob} value (# structural units in a *blob*) remained relatively constant as a function of pyrene content, indicating that the presence of pyrene did not alter the polypeptides behaviour. The N_{blob} values of each polypeptide obtained for different pyrene contents were then averaged and plotted as a function of their comonomer *SCS* in Figure 2A. Figure 2A shows that N_{blob} quickly decreased with increasing *SCS*, reaching a plateau for *SCS* above 4 atoms. A similar trend of decreasing N_{blob} with increasing *SCS* had also been observed with poly(*n*-alkyl methacrylate)s[7] and is thought to be a result of the increasing side chain sterics which led to a straightening of the backbone on the few nm length-scale of a *blob*. The plateau N_{blob} = 11 (±1) value obtained for PGA and PLys(Z)GA indicated that the side chains of GA and Lys(Z) were sufficiently large to fully elongate the polypeptide backbone. Consequently, any side chain containing 5 or more atoms would be expected to affect the backbone in a similar manner. To support this conclusion, molecular mechanics optimizations were conducted on an elongated PGA backbone. By monitoring *in silico* how far apart two pyrenyl labels could be located from one another along an elongated PGA backbone and still form excimer, a theoretical N_{blob}^{theo} value was determined to equal 10 (±1), matching the experimentally determined N_{blob} value.

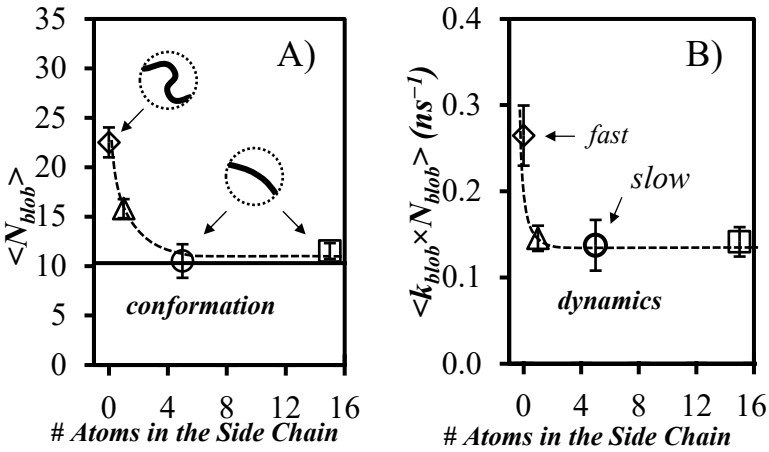

Figure 2. Comparison of the average A) N_{blob} and B) $k_{blob}\times N_{blob}$ values of (◇) Py-PGlyGA, (△) Py-PAlaGA (42 mol% GA), (○) Py-PGA, and (□) Py-Lys(Z)GA in as a function of the number of non-hydrogen side chain atoms in DMSO. The solid line indicates the N_{blob}^{theo} value of 10 ± 1 for an extended polypeptide in a coiled conformation. The dashed lines were added to guide the eyes.

The dynamics of the polypeptides were measured through the term $k_{blob}\times N_{blob}$, which is plotted as a function of *SCS* in Figure 2B. Similar to the trends observed with N_{blob}, $k_{blob}\times N_{blob}$ was largest for PGlyGA and quickly decreased to a plateau with increasing *SCS*. The rapid decrease in $k_{blob}\times N_{blob}$ observed for small *SCSs* indicated that the addition of a fairly small side chain was sufficient to fully stiffen the polypeptide backbone resulting in the near halving of the rate of encounter between the structural units within blobs from 0.26 ns^{-1} for PGlyGA to 0.15 ns^{-1} for PAlaGA. In agreement with the trends of N_{blob}, the plateau of $k_{blob}\times N_{blob}$ at larger *SCSs* meant that incorporation of any comonomer with *SCSs* of 5 atoms or more would result in a copolypeptide exhibiting the same slow dynamics.

Comonomer Composition: The above section demonstrated that the incorporation of a monomer with a small side chain (ex. Gly and Ala) into a polypeptide was able to increase both the conformational freedom and dynamics experienced by the structural units of a polypeptide. However, since all the polypeptide contained ca. 44 mol% of these small comonomers, the relationship between the amount of comonomer and the polypeptides behaviour in solution could not be determined. To address this issue, a series of PAlaGAs (Table 1) were prepared with an

alanine content ranging from 24 to 58 mol%. N_{blob} was found to remain constant with pyrene content, thus demonstrating that the results obtained with the FBM were independent of the pyrene content (x). The effect that the Ala-content had on the chain structure is shown in Figure 3A. Although it was expected that the incorporation of Ala would increase N_{blob}, the response of N_{blob} with respect to the alanine content was rather surprising. Figure 3A shows that the incorporation of 24 mol% Ala into a PGA backbone increased N_{blob} from 11 (±1) to 15 (±1) due to the reduction of side chain sterics. However, upon the further addition of Ala, N_{blob} remained constant taking an average value of 16 ± 1. The constant N_{blob} value of the PAlaGAs indicated that the presence of relatively low levels of Ala were sufficient to entirely disrupt the elongated structure of PGA and therefore the incorporation of more Ala had no effect on the polypeptides conformation. Figure 3B shows that like N_{blob}, $k_{blob}\times N_{blob}$ of the PAlaGAs was more or less independent of the alanine content taking a similar, but slightly larger value compared to that of PGA.

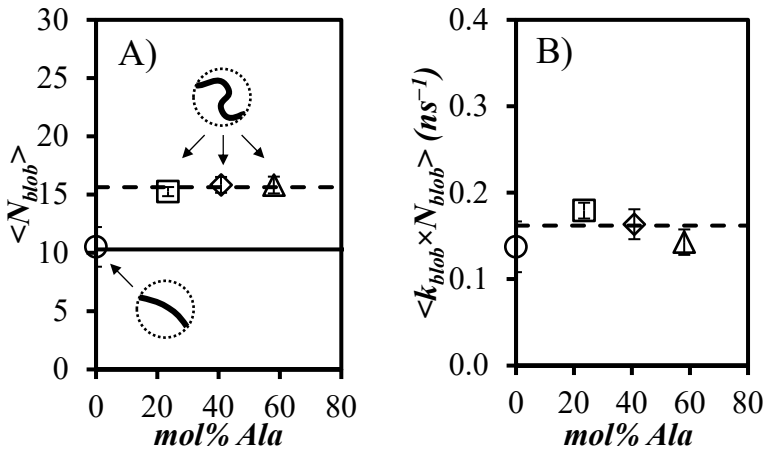

Figure 3: Comparison of A) $<N_{blob}>$ and B) $<k_{blob}\times N_{blob}>$ as a function of (○, 0 *mol% Ala*) Py-PGA and Py-PAlaGAs (*mol% Ala* = (□) 0.24, (◇) 0.41, and (△) 0.58) in DMSO. The dashed lines represent the average values of the Py-PAlaGAs. The solid line indicates the N_{blob}^{theo} value of 10 ± 1.

CONCLUSIONS

The FBM was used to characterize how comonomer size and composition affected the internal dynamics and conformational freedom of copolypeptides. It was found that comonomers with large side chains restricted the backbone freedom of the copolypeptides resulting in the elongation of the backbone and a slowing in the dynamics. A point was reached however where the comonomer was sufficiently large to stiffen the polypeptide on the length-scale of a *blob*, at which point the copolypeptide no longer responded to further increases of the monomer size. Next, the response of a copolypeptide to monomer composition was probed by varying the amount of comonomer incorporated into a polypeptide. Aside from a rapid increase in N_{blob} due to the inclusion of a relatively small (< 25 mol%) amount of flexible comonomer, the solution behaviour of the copolypeptides did not change as a function of comonomer content. This suggested that the flexibility of a copolypeptide is dictated by the smallest (most flexible) comonomer, even if that comonomer had a relatively low incorporation.

REFERENCES

1. Fox, T. G. *Bull. Am. Phys. Soc.* **1956**, *1*, 123.
2. Gordon, M.; Taylor, J. S. *J. Appl. Chem*. **1952**, *2*, 493 – 500.
3. Wood, L. A. *J. Polym. Sci.* **1958**, *28*, 319 – 330.
4. Penzel, E.; Rieger, J.; Schneider, H. A. *Polymers* **1997**, *38*, 325 – 337.
5. Huang, F.; Hudgins, R. R.; Nau, W. M. *J. Am. Chem. Soc.* **2004**, *126*, 16665 – 16675.
6. Leibler, L.; Rubinstein, M.; Colby, R. H. *Macromolecules* **1991**, *24*, 4701– 4707.
7. Farhangi, S.; Weiss, H.; Duhamel, J. *Macromolecules* **2013**, *46*, 9738 – 9747.

Chunxia Tang
Chemical Engineering
Waterloo

Functionalized Cellulose Aerogel Beads for Heavy Metal Ions Removal

Winner of the 2020 IPR Award for Academic Excellence in Polymer Science/Engineering

Functionalized Cellulose Aerogel Beads for Heavy Metal Ions Removal

Chunxia Tang[1], Pritika Brodie[1], Matt Brunsting[2], Kam Chiu Tam[1, *]

1 Department of Chemical Engineering, Waterloo Institute for Nanotechnology, University of Waterloo, 200 University Avenue, Waterloo, ON N2L 3G1, Canada

2 CellScale Biomaterials Testing, 564 Weber St N #11, Waterloo, ON N2L 5C6 Canada

Abstract

Water pollution is a serious issue in the world, which is highly associated with the cumulatively discharge of industry wastewater. Heavy metal ions, such as Cu^{2+}, Pb^{2+}, and Cr^{6+} are among the major components in the industry wastewater, which can threaten human health due to their high toxicity, non-degradability and bio-accumulation. Absorbents, such as activated carbon and petroleum-based polymers are commonly used absorbents or flocculants. However, their low adsorption capacity, high cost, poor recyclability and non-degradability make them a less attractive choice. Therefore, novel absorbents that satisfy all the practical requirements should be developed for future applications.

Developing bio-based absorbents possessing high removal capacity towards heavy metals is one of the key strategies to manage water pollution worldwide. Cellulose is one of the potential alternatives as it is abundant on earth, renewable and bio-degradable. Functionalized cellulose nanofibrils (CNF) as absorbents have been widely reported for wastewater treatment applications due to their larger specific surface area, abundant surface hydroxyl groups and structural flexibility. However, most of the reported cellulose nanomaterial- based absorbents directly used their single fibril form, which are difficult to recover due to their submicron size. Besides, pristine cellulose nanomaterials have low removal capacity due to the low affinity of hydroxyl groups towards heavy metals.

In my PhD research, functional groups are decorated on CNF to improve their metal ions adsorption capacity followed by assembled into aerogels which can be readily separated from the bulk solution. Two cellulose aerogel beads systems are designed depending on the crosslinking

methods and the functional groups. In one study, we grafted a hyperbranched cationic polymer, PEI on CNF using (3-glycidyloxypropyl) trimethoxysilane (GPTMS) as a crosslinker. The obtained mixture was injected into liquid nitrogen for rapid freezing, followed by sublimation to obtain cellulose aerogel beads (diameter between 3-4 mm). The preparation process is shown in Schematic 1. The chemical structure and composition, morphology, mechanical property, Cu (II) ion adsorption capacity and mechanism as well as regeneration performance of the aerogel beads were investigated. The novelty of this work comprise of: (1) cellulose aerogel beads was used instead of cellulose aerogel monoliths for Cu (II) removal to improve the removal efficiency by reducing copper ion diffusion path length; (2) small beads with larger surface to volume ratio than monoliths that enhanced the adsorption rate; (3) a scalable and simple one pot chemical crosslinking reaction conducted at room temperature and in aqueous solution was proposed; (4) the mechanical performance of the aerogel beads were precisely quantified, and to our knowledge, this is the first reported study; (5) the beads possessed excellent adsorption, regeneration and mechanical property, which is very promising for packed column adsorption.

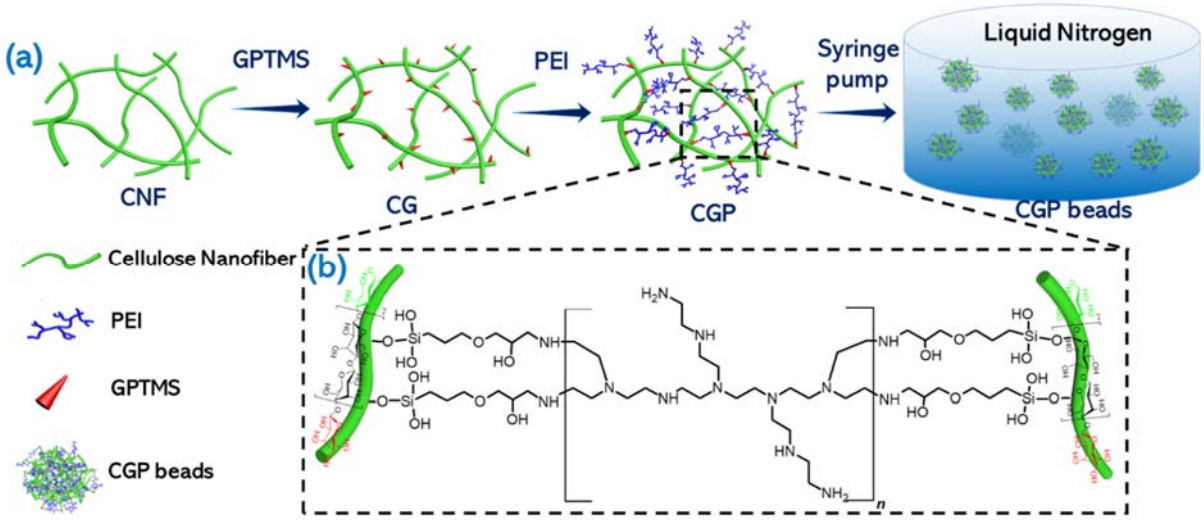

Schematic 1 Illustration of the preparation and chemical structure of the CGP beads

In another study, we developed an efficient and simple and one step procedure to prepare carboxyl decorated and chemically crosslinked CNF aerogel beads. Pristine CNF aerogel beads (average diameter of 3 mm) were prepared by extruding the CNF slurry solution into liquid nitrogen

followed by freeze drying, and maleic anhydride (MA) was used as the crosslinker. The CNF aerogel beads were immersed in maleic anhydride to prepare robust carboxylated CNF aerogel beads. The chemical structure, chemical composition, morphology, mechanical property, Cu (II) ion adsorption capacity and mechanism as well as regeneration performance of the aerogel beads were investigated. The general preparation process and the key concept of this work is illustrated in Schematic 2.

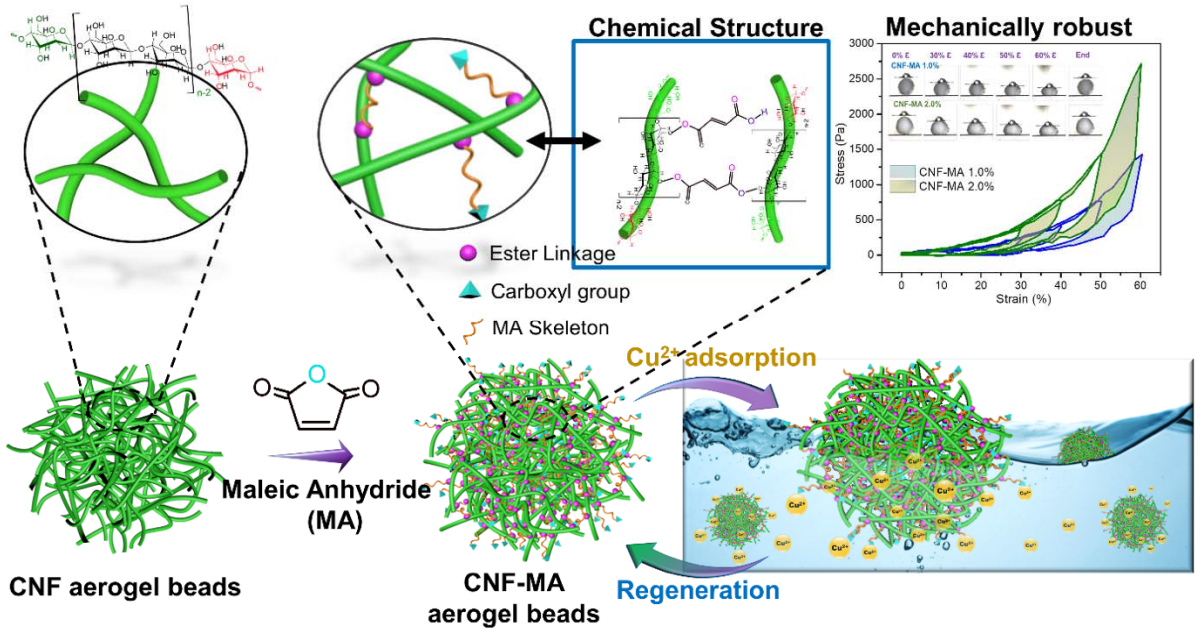

Schematic 2 Illustration of the preparation process, chemical structure and Cu^{2+} removal of the CNF-MA beads

Natun Dasgupta
Chemistry
Waterloo

Thermoresponsive Starch Nanoparticles for Oil Recovery from Tar Sands

Thermoresponsive Starch for Oil Recovery from Tar Sands

Natun Dasgupta and Mario Gauthier

Institute for Polymer Research, Waterloo Institute for Nanotechnology and Department of Chemistry, University of Waterloo, Waterloo, ON N2L 3G1

The bitumen deposits in Canada are considered to be the third largest in the world, at 175-300 billion barrels.[1,2] The Athabasca oil sands lying along the Athabasca River, deposited about 110 million years ago,[3] form the largest bitumen deposit in the world. The sand particles forming the core of the oil sands consist of over 90% quartz with some amounts of potash feldspar, chert and muscovite. Clay minerals also present mostly comprise kaolinite, illite and small amounts of montmorillonite, as shown in Figure 1. Montmorillonite are fine clays with a particle size of less than 44 μm. The porosity of the sand grains is 35% by volume, which allows the bitumen and water contents to be around 18-20% by weight altogether. Oil sands that are rich in bitumen have about 18% bitumen by weight, but on average the bitumen content of Athabasca oil sands is 12%.[3] An oil content of 5-10% is considered intermediate, while sands with 2-5% oil are considered lean.

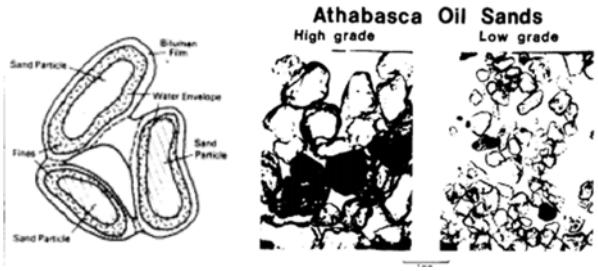

Figure 5. (Left) Cross-sectional view of oil sand particles; (right) bitumen contents in high- and low-grade Athabasca oil sands (the dark spots represent bitumen). Adapted from Ref. 3.

Since bitumen is a heavy oil consisting of large hydrocarbon molecules, the Clark hot water extraction (CHWE) process currently used requires heating water to high temperatures, which consumes a lot of energy with environmental consequences. The procedure also involves harmful chemicals such as sodium hydroxide. Because a limited amount of water can be reused and recycled, this leads to the formation of large tailing ponds of fine sand, oil residues, and several harmful chemicals used in the bitumen extraction process posing great hazard to the environment.

These issues can be tackled by using polymeric surfactants exhibiting a lower critical solution temperature (LCST). These polymers, when coupled with hydrophilic starch nanoparticles, become amphiphilic at temperatures above the LCST. This characteristic can be exploited to extract oil from tar sands without heating the water to high temperatures. Since these smart materials are tunable, characteristics such as the value of the LCST can be controlled. This makes it possible to carry out the extraction process at lower temperatures (45 ^{o}C), but also to reuse the water for multiple cycles of oil extraction. The method developed thus minimizes the use of tailing ponds, protecting life below water and on the land.

Starch is a natural, renewable and biodegradable material consisting of two key polymers: amylose and amylopectin. Amylose is a linear polysaccharide typically making up 15-35% of starch in plants.[4] It has a large number of D-anhydroglucose units attached by α(1→4) glycosidic linkages. Unlike amylose, amylopectin has a highly branched structure including linear segments with α(1→4) glycosidic linkages, but also about 5% of α(1→6)-linkages as branching points. Starch can be isolated from rice, oats, peas, wheat, tapioca, potatoes, corn and other plants.[4] In year 2000, starch production was about 48 million tons per year. Starch is of interest not only as

food, but also to the industry for high-value applications.[5] The use of starch also ensures that these materials are environmentally friendly and non-toxic.

Polysaccharides grafted with thermoresponsive polymers display unique properties, in addition to good biocompatibility and biodegradability. Starch molecules useful for the extraction of oil from tar sands were obtained by modification with thermoresponsive poly(di(ethylene glycol) methyl ether methacrylate) ($PMEO_2MA$) segments through RAFT (reversible addition-fragmentation chain transfer) grafting. $PMEOM_2A$ exhibits an LCST, such that the thermoresponsive polymer-grafted starch is amphiphilic above the LCST and hydrophilic below the LCST. The synthetic methods used provide easy control over the characteristics of the grafted starch (number and length of grafted $PMEO_2MA$ segments), and therefore over their hydrophilic-lipophilic balance (HLB). The starch-*g*-$PMEO_2MA$ samples were characterized by ^1H NMR, UV-visible spectroscopy, TEM and DLS analysis, and the grafted $PMEO_2MA$ chains were cleaved from the starch substrates for analysis by gel permeation chromatography.

Two different strategies were developed to control the characteristics of the target starch-*g*-$PMEO_2MA$ molecules, by using starch modified with suitable functional groups as RAFT agent for the methacrylate monomer (Figure 2). The first approach was to vary the degree of substitution (DS) of the starch-based RAFT agent, while maintaining a constant starch-*g*-$PMEO_2MA$ composition. A RAFT agent with a high DS should indeed generate a larger number of shorter polymer chains due to its multiple reactive sites, while a RAFT agent with a low DS would generate longer polymer chains due to the presence of fewer initiating sites. The other approach was to vary the amount of monomer added to the starch-based RAFT agent for a set DS, since the length of the $PMEO_2MA$ chains should increase with the amount of monomer added to the

reaction. A third approach explored to control the solution properties of the materials was the addition of a block of poly(2-hydroxyethyl acrylate) (PHEA) to form a hydrophilic shell on the particles. It was expected that PHEA, being hydrophilic, may prevent macrophase separation of the thermoresponsive graft polymer above its LCST.

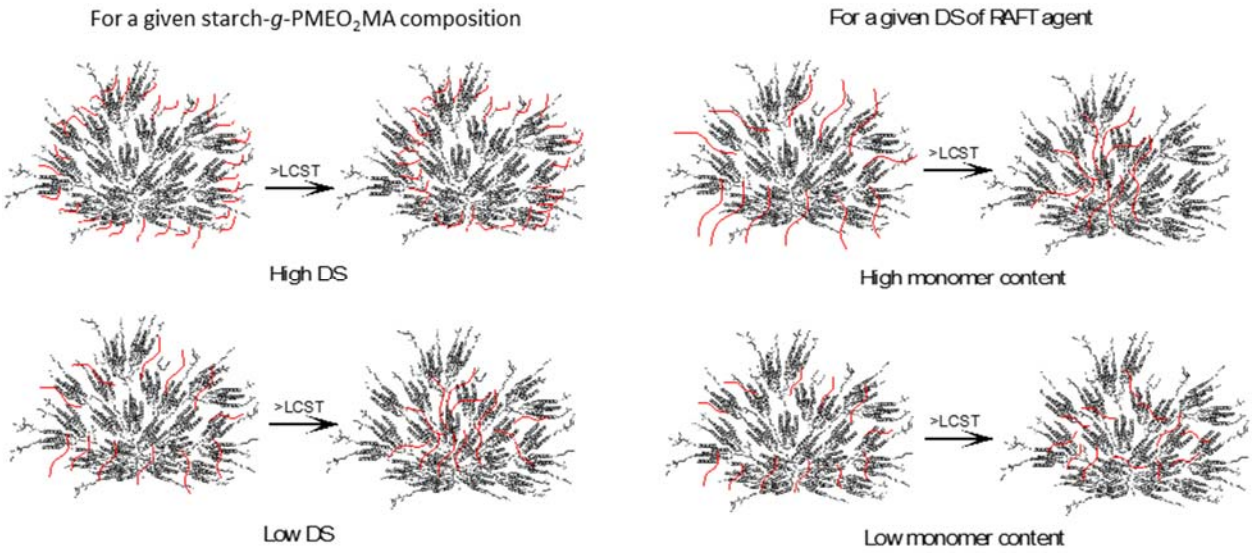

Figure 6. Control of starch-g-PMEO$_2$MA characteristics through variations in the DS of the RAFT agent and the amount of monomer added.

Oil extraction experiments were done using a clamp attached in an oven maintained at 45ºC with 1 g oil sand samples in 20 mL vials as shown in Figure 3. Overall, over 80% extraction efficiency was obtained using starch-*g*-PMEO$_2$MA (15 wt%, DS 0.022) in the presence of 60 mg of toluene, 15 mL of water and 0.5 M NaCl. The extraction efficiency should be higher for lower clay samples. Most importantly, the aqueous phase can be reused in multiple cycles, thus decreasing water and thermoresponsive starch consumption in the extraction process.

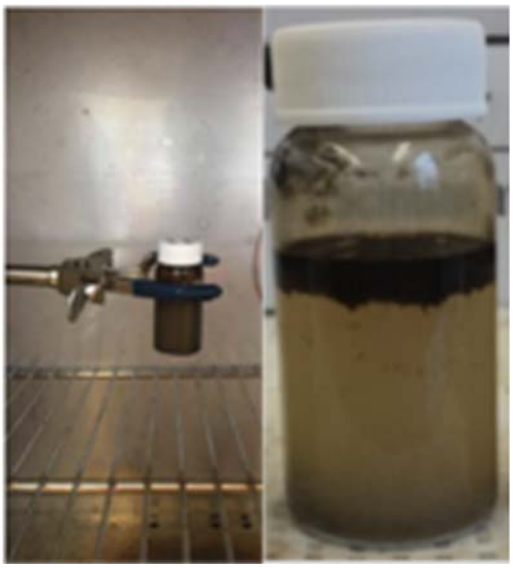

Figure 7. (Left) Vial with 1 g of tar sand (10 ± 1% bitumen content), 15 mg starch-g-PMEO$_2$MA (15 wt%, DS 0.022), 0.5 M NaCl, 60 mg toluene and 15 mL water attached to a tumbler in an oven at 45 °C; (right) bitumen floating on the surface 24 hours after the extraction.

References

(1) Tenenbaum, D. J. Oils Sands Development: A Health Risk Worth Taking? *Environ. Health Perspect.* **2009**, *117* (4).

(2) Masliyah, J.; Zhou, Z. J.; Xu, Z.; Czarnecki, J.; Hamza, H. Understanding Water-Based Bitumen Extraction from Athabasca Oil Sands. *Can. J. Chem. Eng.* **2008**, *82* (4), 628–654.

(3) Takamura, K. Microscopic Structure of Athabasca Oil Sand. *Can. J. Chem. Eng.* **1982**, *60* (4), 538–545.

(4) Ellis, R. P.; Cochrane, M. P.; Dale, M. F. B.; Duffus, C. M.; Lynn, A.; Morrison, I. M.; Prentice, R. D. M.; Swanston, J. S.; Tiller, S. A. Starch Production and Industrial Use. *J. Sci. Food Agric.* **1998**, *77* (3), 289–311.

(5) Le Corre, D.; Bras, J.; Dufresne, A. Starch Nanoparticles: A Review. *Biomacromolecules* **2010**, *11* (5), 1139–1153.

(6) Luzon, M.; Boyer, C.; Peinado, C.; Corrales, T.; Whittaker, M.; Tao, L.; Davis, T. P. Water-Soluble, Thermoresponsive, Hyperbranched Copolymers Based on PEG-Methacrylates: Synthesis, Characterization, and LCST Behavior. *J. Polym. Sci. Part A Polym. Chem.* **2010**, *48* (13), 2783–2792.

(7) Speight, J. G.; Moschopedis, S. E. Factors Affecting Bitumen Recovery by the Hot Water Process. *Fuel Process. Technol.* **1978**, *1* (4), 261–268.

(8) Dai, Q.; Chung, K. H. Bitumen-Sand Interaction in Oil Sand Processing. *Fuel* **1995**, *74* (12), 1858–1864.

Maryam Bagheri
Chemical Engineering
Waterloo

Polysaccharide-Ionic Liquid corrosion inhibitors

POLYSACCHARIDE-IONIC LIQUID AS CORROSION INHIBITORS

BY: MARYAM BAGHERI
SUPERVISOR: PROF LEONARDO SIMON

2020 IPR SYMPOSIUM
UNIVERSITY OF WATERLOO

UNIVERSITY OF WATERLOO

POLYSACCHARIDE APPLICATION

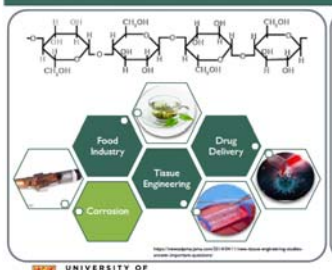

Corrosion Is a Redox Reaction (Oxidation and Reduction)

$$M \longrightarrow M^{+} + e^{-}$$
$$2H^{+} + 2e^{-} \longrightarrow H_2$$
$$O_2 + 2H_2O + 4e^{-} \longrightarrow 4OH^{-}$$

Specification of corrosion inhibitors:

- Ability to form a protective layer on the surface
- Containing hetero atoms (N,S,O)
- Donating their lone pairs of electrons
- Cover a large surface of metal

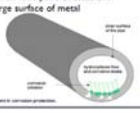

UNIVERSITY OF WATERLOO

MODIFICATION OF POLYSACCHARIDE

Polysaccharide advantages

- **Biosynthetically**
- **Renewability**
- **Biodegradability**
- **Non-Toxicity**

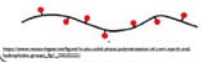

Ionic liquid advantages

- ✓ Low melting point
- ✓ High surface activity
- ✓ Chemical stability
- ✓ Low toxicity
- ✓ High thermal stability
- ✓ Less hazardous influence on environment

Green Chemistry

UNIVERSITY OF WATERLOO

ESTERIFICATION OF DEXTRAN WITH CARBOXYLIC IONIC LIQUID

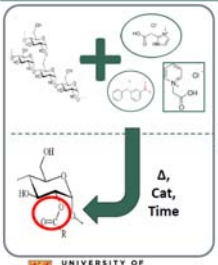

H-NMR Data

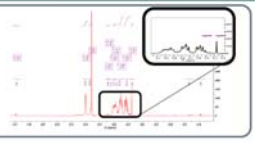

FT-IR Data

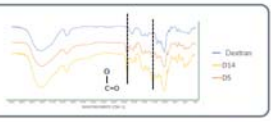

UNIVERSITY OF WATERLOO

EVALUATION INHIBITORS EFFICIENCY

✓ **Potentiodynamic Polarization**

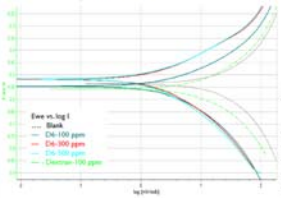

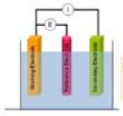

$$\eta_{pol}(\%) = \frac{i_{corr\ blank} - i_{corr\ inhibitor}}{i_{corr\ blank}} \times 100$$

	Concentration (PPM)	E (mV vs. ref)	I (μ A)	Inhibition Efficiency %
Blank	HCl	-550.7	19727	
Dextran	100	-556.4	17340	12.03
D6	100	-552.1	2698	86.3
D6	300	-519.6	1790	90.9
D6	500	-518.8	1638	91.7

Linear polarization diagrams of 1018 steel in 1 M HCl in the absence and presence of different concentration of esterified Dextran at 25 °C.

UNIVERSITY OF WATERLOO

THANK YOU FOR YOUR ATTENTION,
ANY QUESTION?

Ewomazino Ojogbo
Chemical Engineering
Waterloo

Effects of fabrication method on the dispersion of CNCs in highly crosslinked rubber composites

Effect of fabrication methods on the dispersion of CNCs in highly crosslinked rubber composites

by

Ewomazino Ojogbo

Supervised by: Prof. Mekonnen & Prof. Tzoganakis

UNIVERSITY OF WATERLOO
FACULTY OF ENGINEERING

Institute for Polymer Research
IPR
University of Waterloo

Introduction

- Limited practical application of unfilled rubber due to low tensile strength and undesirable responses to weather conditions
- Reinforcing fillers improve properties such as abrasion resistance, tensile, and tear properties
- Typical fillers for rubber include carbon black and silica
- Carbon black riddled with environmental pollution and high energy consumption
- Alternate Filler: Cellulose nanocrystals (CNCs)
- Challenge: Poor dispersion in the rubber matrix due to poor matrix-filler compatibility

UNIVERSITY OF WATERLOO
FACULTY OF ENGINEERING

TEM

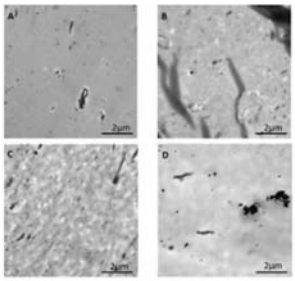

Figure 1. TEM image of unfilled NR (A), 2.5% NR-CNC nanocomposite fabricated by extrusion (B), co-coagulation (C), and batchmixing (D)

UNIVERSITY OF WATERLOO
FACULTY OF ENGINEERING

Tensile strength plots

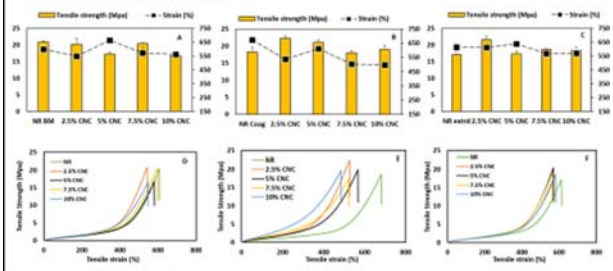

Figure 2: Tensile strength of NR-CNC nanocomposites fabricated by batchmixing (A), co-coagulation (B) and extrusion (C), and Typical tensile strength vs strain plot of NR-CNC nanocomposites fabricated by Batchmixing (D), co-coagulation (E), and extrusion (F)

UNIVERSITY OF WATERLOO
FACULTY OF ENGINEERING

Modulus/ Hardness

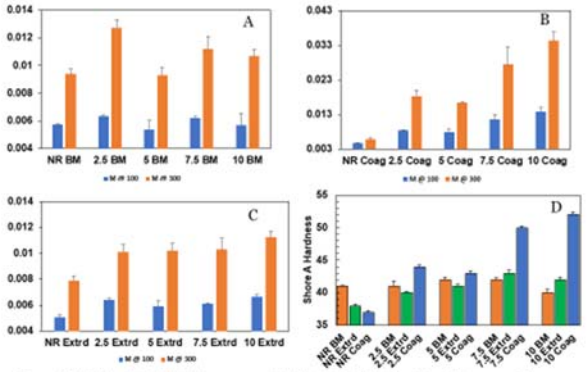

Figure 3. Modulus plot of NR-CNC nanocomposites fabricated (A) batch mixing, (A) co-coagulation, (B) extrusion (C) and Hardness of NR-CNC nanocomposites (D)

Conclusions

- Improved mechanical strength at 2.5% CNC for all fabrication methods
- A decrease in tensile strength observed after 2.5% CNC due to poor dispersion and aggregation of the CNCs in the rubber matrix
- The co-coagualation method of fabrication provided the best mechanical properties

UNIVERSITY OF WATERLOO
FACULTY OF ENGINEERING

Sanjay Patel
Chemistry
Waterloo

Pyrene-labeled Starch Nanoparticles as Fluorescent Sensors for Explosive Detection

Pyrene-labeled Starch Nanoparticles as Fluorescent Sensors for Explosive Detection

By: Sanjay Patel
Supervisor: Jean Duhamel

Current Trends on Explosive Compound Detection

- **Ion mobility spectroscopy**
  → High Sensitivity, high throughput, reliable, robust
- **Canines**
  → Low limit of detections
- **Optical Sensors**
  → Highly portable, quick, typically cost effective

Composed mainly of amylopectin (highly branched)

- Cost effective nanomaterial based on starch

- Readily adsorbs onto polar surfaces, such as filter paper and glass

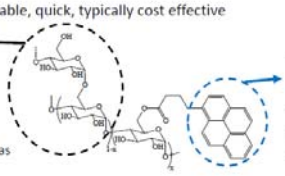

- Well characterized photophysical properties
- Can form excimer
- Hydrophobic
- Commercially available

Time of Detection (TOD)

$$Q_{Eff} = ((1-(\frac{F}{F_0}))\times 100\% = V_{max}(\frac{t}{k_m + t})$$

t= Time (minutes)
V_{max}= Maximum Q_{eff}
k_m= ½V_{max})

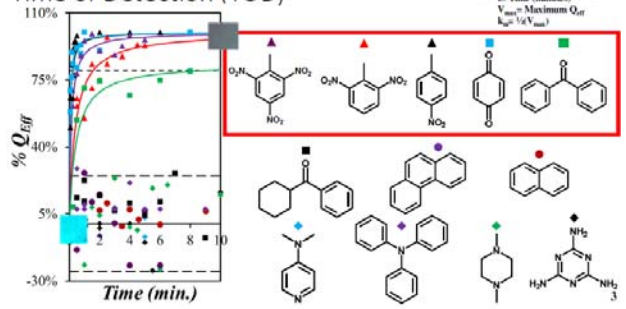

Limit of Detection (LOD)

$$\langle {}^{n}I_{F_0}OSF_0 \rangle / \langle {}^{n}I_{F_P}OSF_P \rangle = 1 - \frac{x^h}{x^h + k^h}$$

x= ng of quencher per mm²
h= Hill coefficient (the steepness)
k= Where 50% quenching occurs

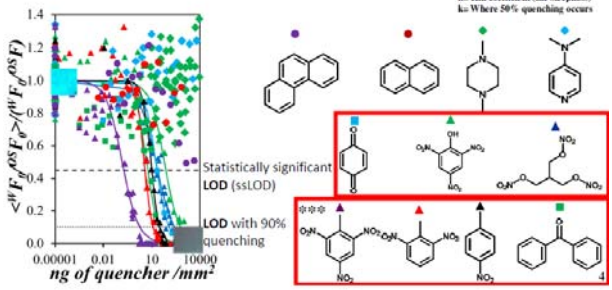

Limit of Detection (LOD)-TNT

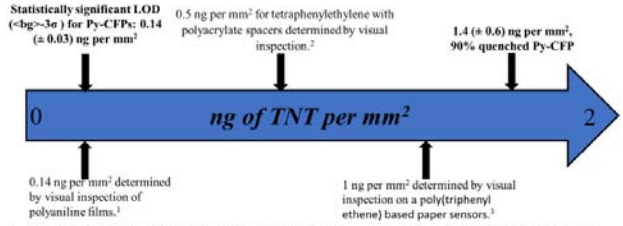

1. Huang, S.; He, Q.; Xu, S.; Wang, L. Polyaniline-Based Photothermal Paper Sensor for Sensitive and Selective Detection of 2,4,6-Trinitrotoluene. *Anal. Chem.* **2019**, *87*, 5451–5456.
2. Li, Q.; Li, X.; Wu, Z.; Sun, Y.; Fang, J.; Chen, D. Highly Efficient Luminescent Side-Chain Polymers with Short-Spacer Attached Tetraphenylethylene AIEgens via RAFT Polymerization Capable of Naked Eye Explosive Detection. *Polym. Chem.* **2018**, *9*, 4150–4160.
3. Zhou, H.; Wang, X.; Lin, T. T.; Song, J.; Tang, B. Z.; Xu, J. Poly(Triphenyl Ethene) and Poly(Tetraphenyl Ethene): Synthesis, Aggregation-Induced Emission Property and Application as Paper Sensors for Effective Nitro-Compounds Detection. *Polym. Chem.* **2016**, *7*, 6809–6817.

Acknowledgements

- Supervisor: Jean Duhamel
- Lu Li and Damin Kim
- The Duhamel Group

6

Donghan Liu
Chemistry
Waterloo

Synthesis and Characterization of Furan Based Non-ionic Surfactant (FBNIOS)

Synthesis and Characterization of Furan Based Non-ionic Surfactants (FBNIOS)

Institute for Polymer Research IPR University of Waterloo

7/29/2020

Presented by: Donghan Liu

Supervisor: Jean Duhamel and Mario Gauthier

UNIVERSITY OF WATERLOO ORIGIN Mitacs NSERC CRSNG

Introduction: Non-ionic Surfactants

- Cost effective
- Retain properties regardless of salt concentration.
- Form non-ionic surfactant liposomes (niosomes)

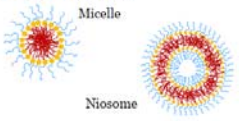

Degree of polymerization by NMR	3	6	10	14
Percentage of chains terminated by *tert*-pentoxide group	4%	5%	5%	3%

Base used: Potassium *tert*-pentoxide
Purification: Column chromatography

UNIVERSITY OF WATERLOO

Steady-State Fluorescence (SSF)

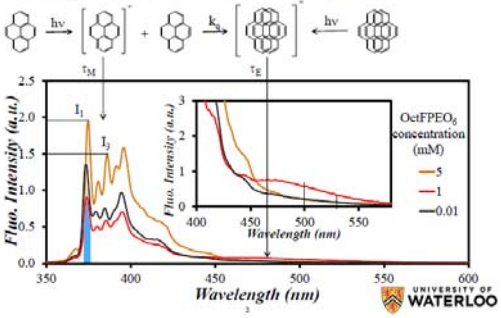

UNIVERSITY OF WATERLOO

C8-F-PEO$_x$ CMC Determination

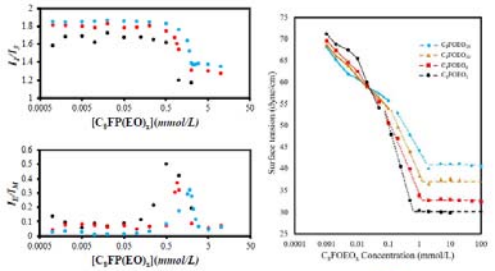

UNIVERSITY OF WATERLOO

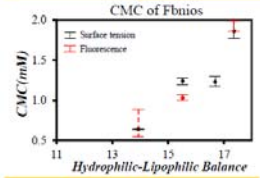

Conclusions

A series of nonionic surfactants were successfully prepared with a hydrophobic octyl chain, a furan core, and hydrophilic oligo(ethylene oxide)s of different lengths. Their CMC was determined by a combination of pyrene fluorescence and surface tension. These nonionic surfactants show properties similar to those of typical surfactants (micelle formation, lower surface tension) but use a furan core obtained from renewable, biodegradable cellulose.

Acknowledgements

- Professors Jean Duhamel and Mario Gauthier
- All group member from Dr. Duhamel's and Dr. Gauthier's lab

Institute for Polymer Research IPR University of Waterloo

Mitacs NSERC CRSNG ORIGIN UNIVERSITY OF WATERLOO

Joanne Fernandez
Chemistry
Waterloo

Grafting of Starch Using a Complex Initiation System of CAN-KPS

Grafting of Starch Using a Cerium–Persulfate Initiation System

Joanne Fernandez and Mario Gauthier

Institute for Polymer Research, Waterloo Institute for Nanotechnology and Department of Chemistry, University of Waterloo, Waterloo, ON N2L 3G1

Introduction

Starch is a biocompatible, renewable and biodegradable polysaccharide. Its abundance and relatively low cost have led to substantial interest in its use as a base material for a wide range of applications.[1] It is composed of two main components, amylose and amylopectin. Amylose is a linear polymer with D-glucopyranose units joined by α-1,4-glucosidic linkages, whereas amylopectin is highly branched with both α-1,4- and α-1,6-glucosidic linkages.[2] The content of amylose and amylopectin in natural starch varies depending on the plant species, but "waxy" starch has essentially no amylose.[1] The characteristics, rheological behaviour and mechanical properties of starch can differ considerably depending on its composition.

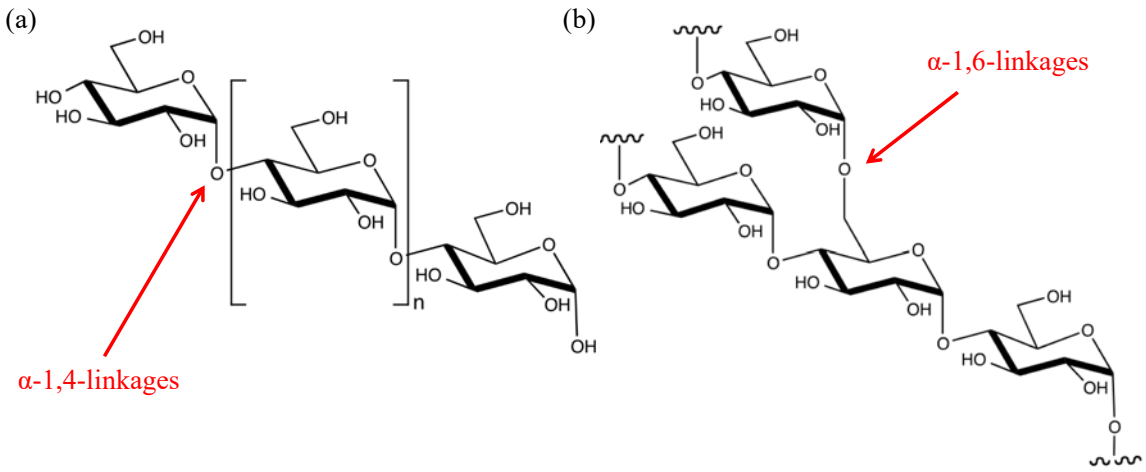

Figure 1. Structure of the starch components (a) amylose and (b) amylopectin.

In its native state, starch has some characteristics that are undesirable for many industrial applications such as poor long-term stability caused by water absorption, and poor mechanical properties.[3] Due to these issues, it cannot be used directly in most cases. Modification by various means, including polymer grafting, is required to achieve more desirable properties. Through modification, starch can acquire characteristics comparable to synthetic petroleum-based

polymers.[4,5] Poly(acrylic acid)-grafted starch, in particular, possesses remarkable water absorbency, and has been used as a platform for controlled drug delivery as well as in paper and textile finishing.[6]

Graft copolymers derived at least in part from renewable resources such as starch have found numerous applications in the industry. The synthesis and properties of various graft copolymers derived from cooked starch, in combination with acrylic acid or acrylonitrile, were explored in this investigation. Initiation was best achieved through a combination of cerium (IV) and potassium persulfate. Grafting of vinyl monomers on starch with cerium (IV) ions is generally assumed to involve a redox initiation process. This is an efficient initiation method, as (ideally) radical centers are formed only on the starch substrate, albeit it is only known to work with a few specific monomers.[7] It was thus determined in the current investigation that acrylic acid could not be grafted directly onto starch using cerium (IV) ions, but the addition of an aldehyde to the reaction enabled grafting with high efficiency. Furthermore, potassium persulfate was introduced to reoxidize the cerium (III) to cerium (IV) in the initiation cycle, thus reducing the amount of initiator required in the reaction.[8] This presentation will focus on the synthesis of poly(acrylic acid)-modified starch and polyacrylonitrile-modified starch via cerium–persulfate initiation and aldehyde-promoted grafting. Various aldehydes were investigated to determine their influence on the grafting efficiency. The modified starch was characterized by nuclear magnetic resonance (NMR) spectroscopy and dynamic light scattering (DLS). In addition, gel permeation chromatography (GPC) was used to determine the molecular weight of the poly(acrylic acid) side chains generated in the grafting reaction.

Experimental

Using an initiation system with cerium (IV) and potassium persulfate, graft copolymers of starch with vinyl monomers were synthesized as shown in Scheme 1.

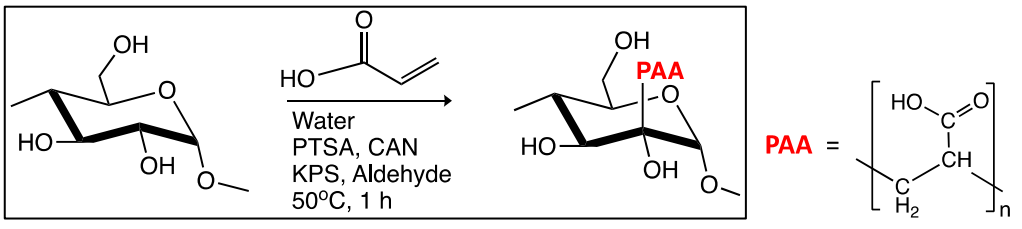

Scheme 1. Synthesis of poly(acrylic acid-modified starch. PTSA: *p*-toluenesulfonic acid; CAN:

ceric ammonium nitrate; KPS: potassium persulfate; PAA: poly(acrylic acid).

The Ce^{4+}/aldehyde redox initiator system (Scheme 2) was also explored to increase the overall grafting efficiency of the reaction.

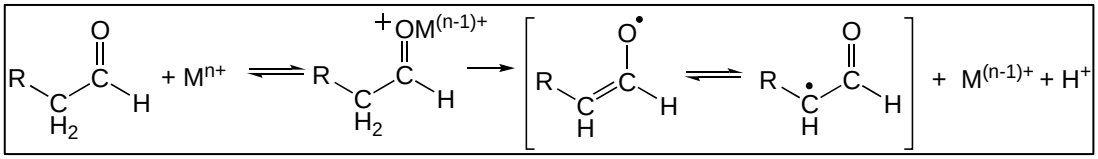

Scheme 2. The Ce^{4+}/aldehyde reaction proceeds through coordination of the carbonyl with loss of an α-hydrogen.

Results and Discussion

The synthesized starch graft copolymers were characterized by various techniques. Through proton nuclear magnetic resonance spectroscopy (Figure 2), the molar substitution of the graft copolymers was determined after purification by dialysis. The peaks at 1.7 and 2.3 ppm are for the $-CH_2-$ and -CH- protons of the poly(acrylic acid) side chains, respectively. The molar substitution achieved was calculated by comparing the integrated values of the side chain peaks with that of the anomeric proton (H_a) on the glucopyranose unit at 5.4 ppm.

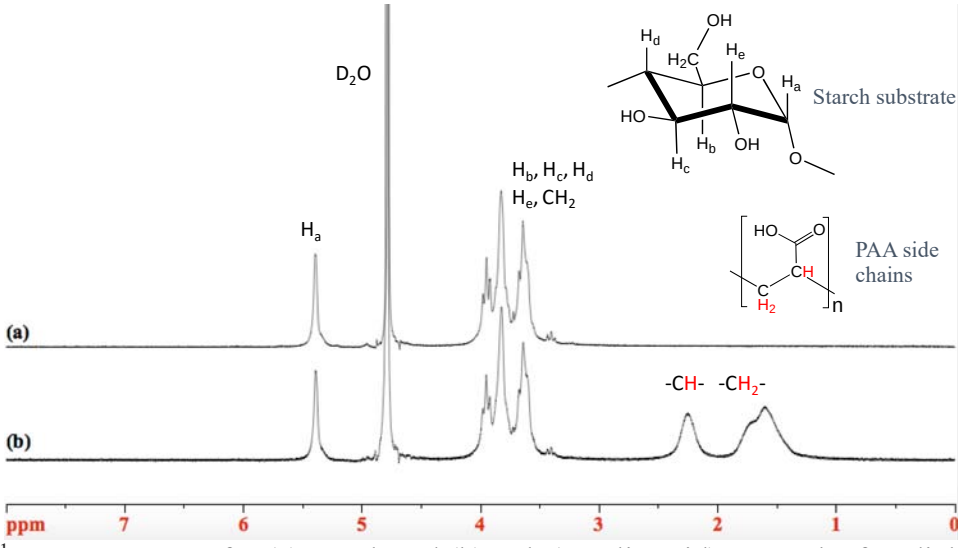

Figure 2. ^1H NMR spectra for (a) starch and (b) poly(acrylic acid)-*g*-starch after dialysis.

Through the addition of various aldehydes (Table 1), it was found that glyoxal and

butyraldehyde both yielded high monomer grafting efficiencies on starch. This correlates with the known relative reactivity of aldehydes RCHO as R = H < phenyl < alkyl.[9]

Table 1. Comparison of the grafting efficiency in the presence of various aldehydes.

Aldehyde	% Monomer conversion (modified starch and homopolymer)	% Monomer grafted to starch	% Monomer converted to homopolymer	Wt% PAA in starch-*g*-PAA
Glyoxal	99 ± 1	82 ± 7	17 ± 7	52 ± 2
Butyraldehyde	97 ± 2	81 ± 9	17 ± 10	52 ± 4
Glutaraldehyde	100 ± 0	59 ± 4	41 ± 4	44 ± 2
Acetaldehyde	80 ± 6	39 ± 2	41 ± 8	34 ± 2

To better understand the effect of glyoxal on the grafting reaction, its concentration was varied from 0 to 8 weight percent with respect to starch. Without glyoxal, poly(acrylic acid) homopolymer was formed but it was not bound to the starch. When glyoxal was introduced in the system, the poly(acrylic acid) chains became bound to the starch substrate.

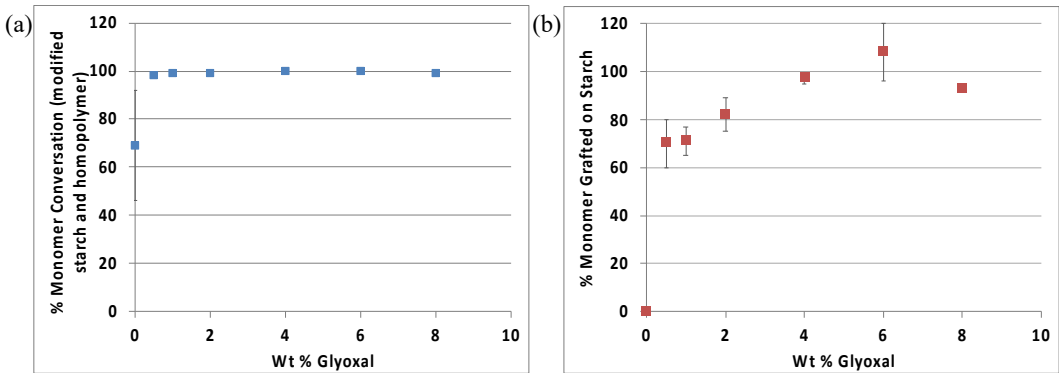

Figure 2. Effect of varying the concentration of glyoxal on (a) the % monomer conversion (modified starch and homopolymer), and (b) the % monomer grafted to the starch.

Conclusions

Graft copolymers of starch with acrylonitrile and acrylic acid were successfully synthesized using a cerium/persulfate initiation system. Through the addition of aldehydes (e.g. glyoxal) to the reaction, the yield of side chains bound to the starch substrate increased markedly. A wider range

of molar substitution levels will be investigated, and further characterization of the graft copolymers by transmission electron microscopy will be carried out.

References

(1) Moad, G. Chemical Modification of Starch by Reactive Extrusion. *Prog. Polym. Sci.* **2011**, *36* (2), 218–237.

(2) Apopei, D. F.; Dinu, M. V.; Dragan, E. S. Graft Copolymerization of Acrylonitrile onto Potatoes Starch by Ceric Ion. *Dig. J. Nanomater. Biostructures* **2012**, *7* (2), 707–716.

(3) Chen, L.; Ni, Y.; Bian, X.; Qiu, X.; Zhuang, X.; Chen, X.; Jing, X. A Novel Approach to Grafting Polymerization of ε-Caprolactone onto Starch Granules. *Carbohydr. Polym.* **2005**, *60* (1), 103–109.

(4) Pourjavadi, A.; Zohuriaan-Mehr, M. J. Modification of Carbohydrate Polymers via Grafting in Air. 1. Ceric-Induced Synthesis of Starch-g-Polyacrylonitrile in Presence and Absence of Oxygen. *Starch/Stärke* **2002**, *54* (3–4), 140–147.

(5) Athawale, V. D.; Vidyagauri, V. L. Graft Copolymerization Onto Starch. 3: Grafting of Acrylamide Using Ceric Ion Initiation and Preparation of Its Hydrogels. *Starch - Stärke* **1998**, *50* (10), 426–431.

(6) Witono, J. R.; Noordergraaf, I. W.; Heeres, H. J.; Janssen, L. P. B. M. Graft Copolymerization of Acrylic Acid to Cassava Starch - Evaluation of the Influences of Process Parameters by an Experimental Design Method. *Carbohydr. Polym.* **2012**, *90* (4), 1522–1529.

(7) Odian, G. *Principles of Polymerization*, 4th ed.; Wiley & Sons: Hoboken, 2004.

(8) Lu, S.; Lin, S.; Yao, K. Study on the Synthesis and Application of Starch-Graft-Poly(AM-Co-DADMAC) by Using a Complex Initiation System of CS-KPS. *Starch - Stärke* **2004**, *56* (34), 138–143.

(9) Mortimer G. A. Chain Transfer in Ethylene Polymerization. VII. Very Reactive and Depletable Transfer Agents. *J Polym Sci Part A-1 Polym Chem* **1972**, *10* (1), 163–168.

Muhammad Shahidul Islam
Chemical Engineering
Waterloo

Cellulose Nanomaterials: Synthesis, Properties, and Applications

Cellulose Nanomaterials: Synthesis, Properties, and Applications

ABSTRACT

Nanotechnology has been recognized as one of the most promising and versatile areas for potential high-tech development in the 21st century. As research advances, the demand for non-petroleum based, carbon neutral biodegradable products from sustainable resources having low environmental, animal/human health and safety risks is ever rising in the field of nanotechnology[1]. The environmental safety issues and the emphasis on "green synthesis (solvent free)" from industries and government have recently generated a significant interest in the development of nanomaterials based on renewable and sustainable natural resources such as cellulose nanocrystals (CNCs) as the alternatives of other polymers or resins. Cellulose is one of the most ubiquitous and abundant renewable biopolymers produced on earth, which is considered as an almost inexhaustible source of raw material to meet the ever-rising demand for a wide spectrum of biocompatible products and materials. Soft and hardwood from higher plants is the most commercially exploited source of cellulose[2].

Considering the increasing interest in sustainability and nanotechnology, the use of CNCs in water treatment applications has gained increasing attention. CNCs have been actively researched for their use in various water treatment systems, such as adsorption, absorption, flocculation, membrane filtration, catalytic degradation and disinfection[3]. CNCs are attractive candidates because of its high specific surface area, high specific strength, hydrophilicity, biodegradability and surface functionalization capabilities[2]. The major types of pollutants present in water bodies include organic dyes, heavy metal ions, pharmaceutics, pesticides, polycyclic aromatic hydrocarbons, and biomolecules. Adsorption is an attractive and economical technique, and when implemented using a well-designed system, it can offer excellent results[3]. The

production of conventional adsorbents, such as activated carbons, can be energy intensive, expensive, and emit greenhouse gases. Thus, producing alternative low-cost adsorbents from industrial and agricultural by-products offers many new opportunities. The use of sustainable nanomaterials, such as CNCs will reduce our dependence on activated carbons and also reduce the carbon foot print as several CNCs based adsorbents have demonstrated excellent adsorption capacity[3].

Cellulose is a long-chain, high molecular weight, and hydrophobic polysaccharide (an isotactic homopolymer) composed of repeat units of dimers or disaccharides of anhydro-D-glucopyranose unit (AGU), known as cellobiose where each anhydro-D-glucopyranose unit is connected by β-1,4 glycosidic linkage and every other monomer is rotated 180^0 with respect to its neighbouring unit (Figure-1A). Cellulose microfibrils are the structural units in the higher plants which are formed by a biogenetic bottom-up process in the nature where the cellulose chains connect or assemble with each other and stabilize through hydrogen bonds and van der Waals forces, further assemblies of fibrils in turn lead to formation of cellulose fibers to form a hierarchical system. These microfibrils, which are several micrometers in length and 5–10 nm in diameter, contain highly ordered (crystalline) regions alternating with disordered (amorphous) regions (Figure-1B and 1C). These crystalline regions can be separated and extracted from the desired cellulose source through a "top down" deconstruction of cellulose fibers by mechanical, chemical or a combination of mechanical, chemical and/or enzymatic (endoglucanases for example) treatments (Figure-1B and 1C), yielding the cellulose nanocrystals (CNCs). The simplest and widely employed process to extract CNCs involves the acid hydrolysis, where concentrated sulphuric acid (H_2SO_4) and hydrochloric acid (HCl) are most commonly used. Sulphuric acid hydrolysis introduces abundant anionic sulfate half ester groups ($–OSO_3^–$) onto the CNC surface

(Figure-1C), which provides electrostatic repulsion among CNC particles in aqueous dispersion and enables the stabilization of CNCs over a wide range of pH values[2]. Currently, the majority of the commercially supplied CNCs (commonly called as the 'Pristine CNC') possess surface – OSO_3^- groups and thus are negatively charged.

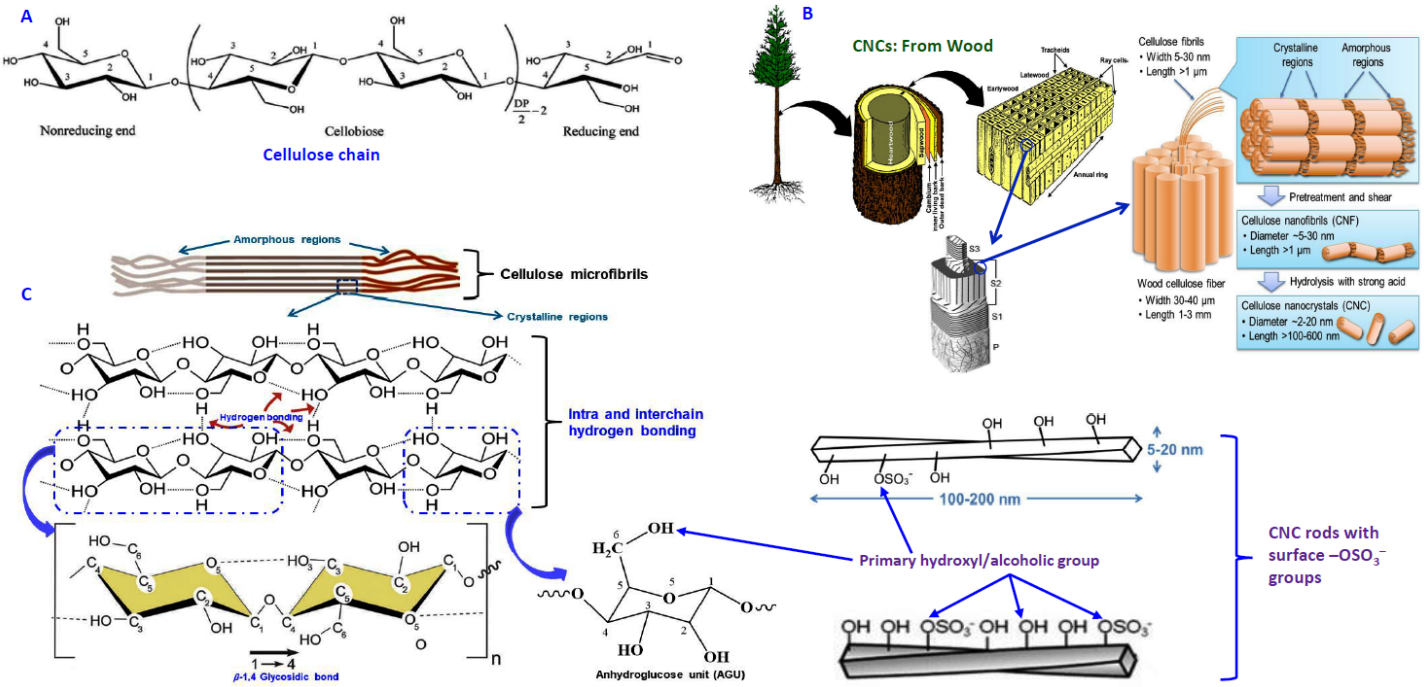

Figure-1: ***(A)*** *Chemical structure of cellulose biopolymer representing reducing and non-reducing ends.* ***B)*** *Schematic illustration of CNC production from fibre cell walls by mechanical and chemical treatments, respectively.* ***C)*** *Amorphous and crystalline portions in cellulose microfibrils, intrachain & interchain hydrogen bonding (dotted line), and the numbering of the carbons in each AGU showing the* 1^0 *alcoholic groups*[2]*. The CNC rods in twisted form at the bottom right corner was adapted from*[4].

In terms of renewability of CNCs, the presence of abundant surface hydroxyl groups enables them for different chemical modification such as oxidation, esterification, etherification, silylation, polymer grafting, etc. (reaction scheme shown in Figure-3). From Figure 1C, it is evident that each AGU of a cellulose chain contain three hydroxyl groups which can be categorized into two chemical class namely, primary (1^0) and secondary (2^0) alcoholic groups. In most instances the hydroxyl groups at the C2 and C3 positions are secondary alcohols while the hydroxyl group in the C6 position is a primary alcohol. Although, the relative reactivity of the hydroxyl groups has the following order; (C6)–OH >> (C2)–OH > (C3)–OH, but most of the modification occurs at the (C6)–OH[5]. Such potential chemical modifications also allow their incorporation and dispersion into different hydrophilic/hydrophobic polymer matrices effectively rendering CNCs the status of an ideal candidate as a novel material[5].

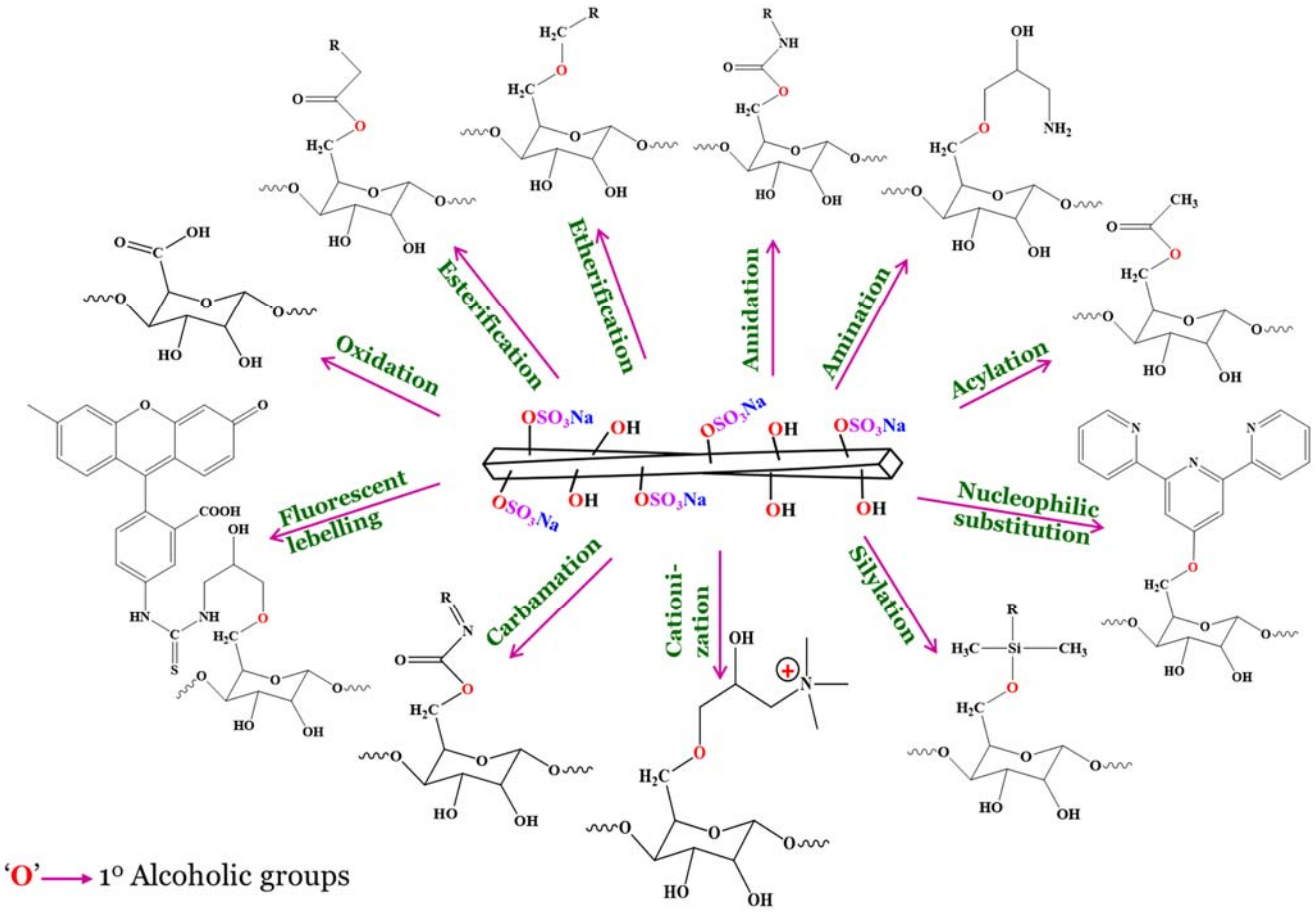

Figure-2: *Surface functionalization of CNCs through various covalent modifications.*

Currently, the three major suppliers of pristine CNCs are –

- CelluForce Inc: the world's largest producer of CNCs (NCC^{TM}),
- Alberta Innovates Technology Futures (AITF), and
- USDA (U.S. Department of Agriculture) Forest Products Laboratory (FPL).

As the majority of the surface 1^0 alcoholic groups are occupied by $–OSO_3^-$ groups in the pristine CNCs (reported S = 0.86 %, w/w)[6], and the chemical modification(s) preferably occurs at the 'free' 'most reactive' 1^0 alcoholic group(s) on C6 protruding from the CNC rods, desulfation of such pristine CNC is necessary prior to any chemical modification.

CNCs are the unique nanomaterials among the other nanomaterials of the same range due to its exceptional properties discussed above. Due to its nanoscale size, high aspect ratio, and unique mechanical and chemical properties, CNCs have a plethora of applications notably in the paper, polymer, plastics, chiral templating, flocculants, aerogels, hydrogels, materials science, electronics, drug delivery, cosmetics, pharmaceuticals and tissue engineering.

REFERENCES

1. Moon, R. J., Martini, A., Nairn, J., Simonsen, J. & Youngblood, J. *Cellulose nanomaterials review: structure, properties and nanocomposites*. *Chemical Society Reviews* **40,** (2011).
2. Islam, S., Chen, L., Sisler, J. & Tam, K. C. Cellulose Nanocrystal (CNC) – Inorganic Hybrid Systems: Synthesis, Properties and Applications. *J. Mater. Chem. B* **6,** 864–883 (2018).
3. Grishkewich, N., Mohammed, N., Tang, J. & Tam, K. C. Recent advances in the application of cellulose nanocrystals. *Curr. Opin. Colloid Interface Sci.* **29,** 32–45 (2017).
4. Hu, Z., Ballinger, S., Pelton, R. & Cranston, E. D. Surfactant-enhanced cellulose nanocrystal Pickering emulsions. *J. Colloid Interface Sci.* **439,** 139–148 (2015).
5. Habibi, Y., Lucia, L. A. & Rojas, O. J. Cellulose nanocrystals: Chemistry, self-assembly, and applications. *Chem. Rev.* **110,** 3479–3500 (2010).
6. Akhlaghi, S. P. *et al.* Synthesis of amine functionalized cellulose nanocrystals: Optimization and characterization. *Carbohydr. Res.* **409,** 48–55 (2015).

Damin Kim
Chemistry
Waterloo

Better Understanding the Structure of Glycogen with Pyrene Excimer Fluorescence

Characterization of the Conformation of Glycogen in Solution by Pyrene Excimer Fluorescence

Damin Kim and Jean Duhamel
IPR Symposium, University of Waterloo, Waterloo, ON, N2L 3G1, Canada

Introduction

Glycogen is a major carbohydrate that animals and humans alike use as energy storage. The structure of glycogen has been investigated for many years. Glycogen is a polysaccharide made of linear segments of anhydroglucose units (AGUs) joined by α-(1,4) glycosidic bonds. These oligosaccharides are connected to each other by α-(1,6) glycosidic bonds. The general structure of glycogen is similar to that of amylopectin, the main carbohydrate used for energy storage by plants. However, the degree of branching of glycogen is twice larger than for amylopectin. Following the suggestion by Whelan in 1970 that glycogen could be viewed as a sphere made of concentric tiers,[1] the Tier Model was proposed. The fundamental purpose of the Tier Model was to explain how glycogen could store about 55,000 glucose units inside a sphere with a diameter of 40 nm.[2] The Tier Model uses the degree of polymerization, or chain length (*CL*), of the side chains constituting glycogen. *CL* can vary from 9 to 16 AGUs depending on the source of glycogen.[3] The molecular weight of glycogen can be calculated with Equation 1 where 162 g/mol, *r*, and *t* represent the molar mass of an AGU, the degree of branching, and the number of tiers. Degrees of branching higher than 2 result in densities that are much too high for glycogen. After optimization, the degree of branching was found to equal 2 (i.e. $r = 2$ in Equation 1).[4]

$$M_n = 162 \times \left(\frac{1 - r^t}{1 - r} \times CL \right) \tag{1}$$

Considering that each AGU increases the tier thickness (*tt*) by 0.126 nm and that the branching point generated by an α-(1,6) glycosidic bond adds 0.35 nm to *tt*,[5] *tt* could be calculated according to Equation 2.

$$tt = 0.126 \times CL + 0.35 \tag{2}$$

The density (ρ) of a glycogen molecule made of *t* tiers can then be calculated with Equation 3.

$$\rho = \frac{3 \times 162 \times CL}{4\pi (t \times tt)^3 \times N_A} \quad \text{it is wrong wrong} \tag{3}$$

X-ray crystallography has demonstrated that the crystalline lamellae of amylopectin are constituted of mainly double helices that are hexagonally packed.[6] Assuming that the oligosaccharide branches of glycogen form helices that also pack hexagonally, the density of each tier can be calculated with Equation 4 where $d_{\text{h-h}}$ is the interhelical distance.

$$\rho_{tier} = \frac{162 \times CL}{N_A \left(\frac{\tan(\pi/3)}{2} d_{h-h}^2 \times tt \right)} = \frac{162 \times CL \times r^{t-1}}{\frac{4\pi}{3} \times tt^3 \left(t^3 - (t-1)^3 \right)} \tag{4}$$

A hypothetical glycogen molecule made of 13 tiers would be too dense and would leave no room in the peripheral tier for an enzyme to enter the glycogen macromolecular volume and graft a new oligosaccharide branch or depolymerize the polysaccharide into AGUs. Therefore, the maximum number of tiers that glycogen can have is 12.[3]

Two glycogen samples, one extracted from oyster and the other from corn (phytoglycogen), were probed by a combination of pyrene excimer fluorescence (PEF), fluorescence blob model (FBM), and molecular mechanics optimizations (MMOs) to assess the validity of the Tier Model proposed for glycogen. Gel Permeation Chromatography and intrinsic viscosity measurements were also conducted to determine the molecular weight and density of glycogen, respectively.

Experimental

Materials: Glycogen from oyster (Type II) was purchased from Sigma Aldrich and phytoglycogen was generously donated by Mirexus. Glycogen from oyster and corn were used after precipitation in ethanol. All other chemicals involved in the pyrene-labeling reaction were purchased from Sigma and used without any purification.

Labeling of Glycogen with 1-Pyrenebutyric Acid: Esterification, purification, and characterization of pyrene-labeled glycogen was conducted in the same manner as described earlier for pyrene labeled nanosized amylopectin fragment.[7] The only modification added to the procedure was the temperature at which glycogen was dispersed in DMSO. Glycogen was dispersed in DMSO at 80 ^{o}C compared to 60 ^{o}C for nanosized amylopectin fragments.

Results and Discussion

The molecular weight distribution of unlabeled glycogen from oyster and corn was determined by gel permeation chromatography in DMSO. The number average molecular weight (M_n) of glycogen from oyster and corn equaled 4.1×10^6 and 8.5×10^6 g/mol, respectively. Both glycogens exhibited a narrow molecular weight distribution with a PDI of 1.02 for glycogen from oyster and 1.15 for phytoglycogen. The intrinsic viscosity ($[\eta]$) of glycogen from oyster was determined with an Ubbelohde viscometer to equal 9.1 ± 0.5 mL/g. The pressure detector on the GPC was used to determine $[\eta]$ for phytoglycogen found to equal 7.8 ± 0.5 mL/g. Using the known *CL* of 10 and 12 for, respectively, glycogen from oyster[2] and corn,[8] the number of tiers, that each glycogen molecule was made of, could be calculated according to Equation 3. The results of these calculations are listed in Table 1.

Table 1. Number of tier in glycogen determined by intrinsic viscosity, GPC and fluorescence.

	Experimentally determined # Tier			
	Intrinsic Viscosity	GPC	Fluorescence	Average
Glycogen from oyster	11.3	11.2	12.2	11.6 (± 0.8) ~12
Phytoglycogen	12.2	12.6	12.6	12.2 (± 0.3) ~12

The glycogen samples were further investigated by GPC. The average hydrodynamic radius (R_h) of glycogen equaled 18.1 (±0.3) nm for oyster and 23.5 (± 1.9) nm for phytoglycogen. The difference in size could be attributed to the different *CL* values which have been reported to equal 10 and 12 AGUs for glycogen from oyster[3] and corn,[8] respectively. According to Equation 2, these *CL* values imply a *tt* of 1.61 and 1.86 nm for glycogen from oyster and corn, respectively. In turn, they would suggest a number (*t*) of tiers given by the ratio R_h/tt equal to 11.2 (±0.2) and 12.6 (±1.0) for glycogen from, respectively, oyster and corn, in excellent agreement with the *t* values obtained by $[\eta]$ measurements (see 1st column in Table 1). The shape factor given by the ratio of the radius

of gyration over R_h (R_g/R_h) equaled 0.86 and 0.94 for glycogen from oyster and corn, respectively. Hyperbranched polymers generally have a shape factor between 0.98 and 1.2.[9] Glycogen from oyster had a somewhat lower value than expected for hyperbranched polymers, but it agreed with other R_g/R_h reported in the literature.[10] The Mark Houwink Sakurada (MHK) exponent was found to equal 0.34 for phytoglycogen. This exponent was similar to that of amylopectin reflecting the highly branched nature of glycogen.[11,12] The MHS exponent was also smaller than 0.5 which is what would be expected for a polymer in a θ-solvent.[13] The small exponent of 0.34 confirmed the compact nature of phytoglycogen due to its highly branched architecture.

The validity of the Tier Model was further investigated for glycogen by PEF. The two glycogen samples were labeled with different amounts of pyrene. The fluorescence spectra were acquired for the pyrene-labeled glycogen samples and they are shown in Figure 1A for glycogen from oyster. As the pyrene content increased, more pyrene-pyrene encounters took place in solution and more excimer was formed resulting in an increase in the fluorescence intensity of the excimer at 480 nm with respect to that of the monomer at 378 nm. This effect could be quantified by plotting the ratio of the fluorescence intensity of the pyrene excimer (I_E) over that of the monomer (I_M) as shown in Figure 1B. The I_E/I_M ratio increased continuously with increasing pyrene content in Figure 1B reflecting the increase in local pyrene concentration experienced by an excited pyrene. Interestingly, the I_E/I_M ratios for glycogen obtained from oyster or corn overlapped at a same pyrene content. This observation indicated that at the molecular level, an excited pyrenyl label experienced a same environment for both glycogen samples suggesting that both samples had a similar interior.

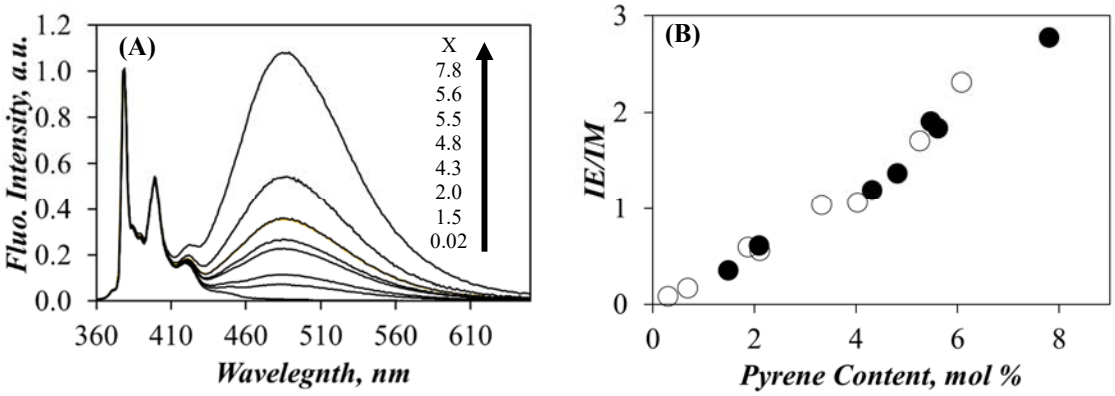

Figure 1. (A) Emission spectra of glycogen from oyster labeled with different pyrene contents (*x* increasing from 0.02 to 7.8) (B) I_E/I_M ratio as a function of pyrene content for pyrene-labeled glycogen from oyster (●) and from corn (○).

While interesting, the I_E/I_M ratios only allow a somewhat limited analysis of the fluorescence response for any pyrene-labeled macromolecule because it combines two effects. Indeed, PEF depends on first, the conformation of the macromolecule in solution, a denser conformation bringing the pyrenyl labels closer from each other and resulting in stronger PEF, and second, the flexibility of the polymeric backbone, a stiffer backbone hindering pyrene-pyrene encounters and resulting in less efficient PEF. This is when the fluorescence blob model (FBM) analysis of fluorescence decays acquired with a macromolecule randomly labeled with pyrene comes into play. The FBM assumes that the macromolecular volume can be compartmentalized into *blobs* among which the pyrene labels distribute themselves randomly according to a Poisson distribution. FBM analysis of the fluorescence decays yield the parameters N_{blob} and k_{blob}. k_{blob} is the rate

constant of PEF and reflects the flexibility of the macromolecular backbone while N_{blob} is the number of structural units of the macromolecule found inside a *blob*. N_{blob} is thus a measure of the internal density of the macromolecule.

An earlier study applied PEF to determine that amylose adopts a helical conformation in DMSO.[14] To reach this conclusion, the N_{blob} value of 10 ± 1 found for pyrene-labeled amylose in DMSO was compared to that of a molecular model built with HyperChem for pyrenyl labels covalently attached onto an amylose helix. The theoretical N_{blob} (N_{blob}^{theo}) found by conducting molecular mechanics optimization (MMOs) to probe the maximal number of AGUs separating two pyrenyl labels and still allowing PEF was found to equal 11, in perfect agreement with the experimental N_{blob} of 10 ± 1. The good agreement between the experimental and theoretical N_{blob} values indicated that amylose adopted a helical conformation in DMSO. These PEF experiments were repeated with the pyrene-labeled glycogens and the N_{blob} values retrieved by applying the FBM analysis to the fluorescence decays were plotted as a function of pyrene content in Figure 2 A. Within experimental error, N_{blob} remained constant with pyrene content and regardless of the origin of the glycogen sample. It equaled 41 (±3), a much larger value than for amylose with an N_{blob} value of 10 ± 1. The four-fold larger N_{blob} value obtained for glycogen compared to amylose indicated that the environment probed by an excited pyrene was much denser for glycogen than for amylose.

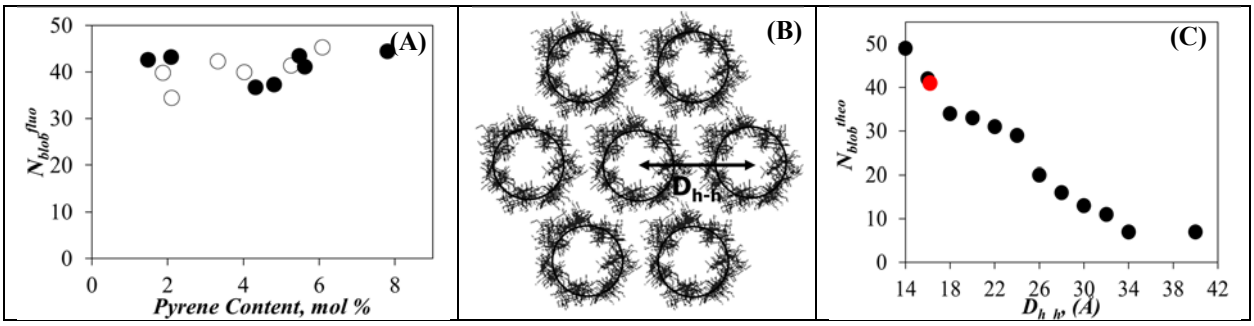

Figure 2. (A) Plot of N_{blob} as a function of pyrene content for pyrene-labeled glycogen from oyster (●) and corn (○) (B) Illustration of the hexagonal arrangement for the glycogen helices. (C) Plot of N_{blob}^{theo} (●) as a function of d_{h-h} and the experimentally determined N_{blob}(●).

As for amylose, MMOs were conducted with Hyperchem to determine N_{blob}^{theo} for glycogen. An oligosaccharide helix was built with 10 AGUs. Since the primary alcohol is more reactive than the secondary alcohol, 1-pyrenebutyric acid was attached to the C6 hydroxyl of the AGU. The reference pyrene was attached to the AGU located at the top of the helix and the secondary pyrene was attached onto the next AGU and the two pyrenes were induced to overlap. A pair of pyrenes, where one of the pyrenes had more than 6 carbons overlapping the frame of the other pyrene, was considered to result in PEF. The largest number of AGUs separating two pyrene labels while still allowing PEF was taken as N_{blob}^{theo}. N_{blob}^{theo} for PEF taking place inside a same helix equaled 6.5 ± 0.5 AGU. Assuming that the glycogen helices were arranged in a hexagonal array, N_{blob}^{theo} was determined as a function of the interhelix distance (d_{h-h}) when PEF occurred between two pyrenyl labels attached on two different helices. The reference pyrene was attached on the helix located at the center of the hexagonal array shown in Figure 2B and the second pyrene was attached on one of the adjacent helices. When d_{h-h} was greater than 34 Å, PEF could not take place between helices

and N_{blob}^{theo} equaled 7. Upon decreasing $d_{h\text{-}h}$, more anhydroglucose units were included in the calculation of N_{blob}^{theo} and N_{blob}^{theo} was shown to increase quickly with decreasing $d_{h\text{-}h}$ in Figure 2C. When $d_{h\text{-}h}$ equaled 16.2 Å, the experimental N_{blob} matched N_{blob}^{theo}.

Equating each side of Equation 4 for the density of each tier (ρ_{tier}) using a $d_{h\text{-}h}$ value of 16.2 Å yielded *t* which was found to equal 12.2 and 12.6 for glycogen from oyster and corn, respectively. This derivation assumed that pyrene targets preferentially the parts of glycogen that are denser in AGUs located mainly at the periphery of the molecule. The *t* values obtained by a combination of PEF, FBM, and MMOs were in perfect agreement with those found by [η] and GPC measurements.

Conclusions

Glycogen was obtained from two different sources and the number of tiers constituting both glycogen samples were investigated with three different techniques including GPC, [η], and PEF. The three techniques confirmed that these glycogen samples contained 12 tiers, regardless of the source of glycogen. This study represents the first example where PEF was applied to demonstrate the applicability of the Tier Model for glycogen. The PEF study yielded the interhelical distance in the 12th outer tier of glycogen equal to 16.2 Å.

References

1. Gunja-Smith, Z.; Marshall, J. J.; Merciere, C.; Smith, E. E.; Whelan, W. J. *Febs. Lett.* **1970***, 12,* 101-104.
2. Madsen, M. B.; Cori, C. F. *J. Biol. Chem.* **1958***, 233,*1251-1254.
3. Manner, D. J. *Carbohydr. Polym.* **1991**, *16*, 37-82.
4. Melendez-Hevia, E.; Waddell, T. G.; Shelton, E. D. *Biochem. J.* **1993***, 295,* 477-483.
5. Goldsmiths, E.; Sprang, S.; Fletterick, R. *J. Mol. Biol*. **1982**, *156*, 411-427.
6. Pérez, S.; Bertoft, E. The molecular structures of starch components and their contribution to the architecture of starch granules: A comprehensive review. *Starch* **2010**, *62*, 389-420.
7. Zhang, Q.; Kim, D.; Li, L.; Patel, S.; Duhamel, J. *Langmuir* **2019**, *35*, 3432-3444.
8. Yun, S. H.; Metheson, N. K. *Carbohydr. Res.* **1993**, *243*, 307–321.
9. Striegel, A. M.; Kirkland, J. J.; Yau, W. W.; Bly, D. D. Modern Size-Exclusion Liquid Chromatography-Practice of Gel Permeation and Gel Filtration Chromatography. 2nd Ed. New Jersey: John Willey Sons, 2009.
10. Ioan, C. E.; Aberle, T.; Burchard, W. *Macromolecules* **1999**, *32*, 7444-7453.
11. Millard, M. M.; Dintzis, F. R.; Willett, J. L.; Klavons, J. A. *Cereal Chem*. 1997, 74, 687-691.
12. Ma, Z.; Zhao, S.; Cheng, K. ; Zhang, X. ; Xu, X. ; Zhang, L. *J. Appl. Polym. Sci*. 2007, 104, 3124-3128.
13. Hill, S. E.; Ledward, D. A.; Mitchell, J. R. Functional Properties of Food Macromolecules. 2nd Ed. Maryland: An Aspen Publication, 1998.
14. Li, L.; Duhamel, J. *Macromolecules* **2016**, *49*, 7965-7974.